Rota *et al. eLight* (2024) 4:13
https://doi.org/10.1186/s43593-024-00072-8

Official Journal of CIOMP
elight.springeropen.com

RESEARCH ARTICLE

Open Access

A source of entangled photons based on a cavity-enhanced and strain-tuned GaAs quantum dot

Michele B. Rota[1†], Tobias M. Krieger[2†], Quirin Buchinger[3], Mattia Beccaceci[1], Julia Neuwirth[1], Hêlio Huet[1], Nikola Horová[4], Gabriele Lovicu[1], Giuseppe Ronco[1], Saimon F. Covre da Silva[2,5], Giorgio Pettinari[6], Magdalena Moczała-Dusanowska[3], Christoph Kohlberger[2], Santanu Manna[2], Sandra Stroj[7], Julia Freund[2], Xueyong Yuan[2,8], Christian Schneider[9], Miroslav Ježek[4], Sven Höfling[3], Francesco Basso Basset[1], Tobias Huber-Loyola[3*], Armando Rastelli[2*] and Rinaldo Trotta[1*]

Abstract

A quantum-light source that delivers photons with a high brightness and a high degree of entanglement is fundamental for the development of efficient entanglement-based quantum-key distribution systems. Among all possible candidates, epitaxial quantum dots are currently emerging as one of the brightest sources of highly entangled photons. However, the optimization of both brightness and entanglement currently requires different technologies that are difficult to combine in a scalable manner. In this work, we overcome this challenge by developing a novel device consisting of a quantum dot embedded in a circular Bragg resonator, in turn, integrated onto a micromachined piezoelectric actuator. The resonator engineers the light-matter interaction to empower extraction efficiencies up to 0.69(4). Simultaneously, the actuator manipulates strain fields that tune the quantum dot for the generation of entangled photons with corrected fidelities to a maximally entangled state up to 0.96(1). This hybrid technology has the potential to overcome the limitations of the key rates that plague QD-based entangled sources for entanglement-based quantum key distribution and entanglement-based quantum networks.

[†]Michele B. Rota and Tobias M. Krieger have contributed equally to this work.

*Correspondence:
Tobias Huber-Loyola
tobias.huber@physik.uni-wuerzburg.de
Armando Rastelli
armando.rastelli@jku.at
Rinaldo Trotta
rinaldo.trotta@uniroma1.it
[1] Dipartimento di Fisica, Sapienza University of Rome, Piazzale Aldo Moro 5, 00185 Rome, Italy
[2] Institute of Semiconductor and Solid State Physics, Johannes Kepler University, Altenberger Strasse 69, 4040 Linz, Austria
[3] Technische Physik, Universität Würzburg, Am Hubland, 97074 Würzburg, Germany
[4] Department of Optics, Faculty of Science, Palacký University, 17. Listopadu 1192/12, 77900 Olomouc, Czech Republic
[5] Present Address: Instituto de Física Gleb Wataghin, Universidade Estadual de Campinas, 13083-859 Campinas, Brazil
[6] Institute for Photonics and Nanotechnologies, National Research Council, Via del Fosso del Cavaliere, 100, 00133 Rome, Italy
[7] Research Center for Microtechnology, Vorarlberg University of Applied Sciences, Campus V, Hochschulstrasse 1, 6850 Dornbirn, Austria
[8] Present Address: School of Physics, Southeast University, Nanjing 211189, China
[9] Institut für Physik, Fakultät V, Carl von Ossietzky, Universität Oldenburg, 26129 Oldenburg, Germany

Springer Open

© The Author(s) 2024. **Open Access** This article is licensed under a Creative Commons Attribution 4.0 International License, which permits use, sharing, adaptation, distribution and reproduction in any medium or format, as long as you give appropriate credit to the original author(s) and the source, provide a link to the Creative Commons licence, and indicate if changes were made. The images or other third party material in this article are included in the article's Creative Commons licence, unless indicated otherwise in a credit line to the material. If material is not included in the article's Creative Commons licence and your intended use is not permitted by statutory regulation or exceeds the permitted use, you will need to obtain permission directly from the copyright holder. To view a copy of this licence, visit http://creativecommons.org/licenses/by/4.0/.

1 Introduction

Scalable sources of entangled photons are the keystone for the realisation of a photonic quantum network [1–5] where quantum bits of information are, for example, encoded in the polarization state of single photons and travel between different nodes of the network [6]. To date, the majority of entanglement-based quantum communication protocols have been implemented using sources based on spontaneous parametric down-conversion (SPDC) processes [7, 8]. SPDC sources can generate high-fidelity entangled photons with high brightness and provide the possibility of exploiting entanglement on different degrees of freedom [9, 10]. However, they are fundamentally limited by their probabilistic emission [11, 12] which can reduce the maximal rate of operation and hinder scaling up to large photon number applications [9].

Quantum emitters driven under resonant excitation have instead the potential to overcome these hurdles: because of the Pauli exclusion principle and Coulomb interaction, each excited state can be populated only once, and the simultaneous emission of more than one photon of a given frequency per excitation cycle is reduced to the negligible probability of re-excitation during the same laser pulse [13, 14]. Moreover, the use of a resonant excitation scheme with near-unity preparation fidelity [15–17] opens the possibility of achieving on-demand photon generation.

Among the plethora of quantum emitters available to date, e.g., colour centres in diamond [18], and defects in 2D materials [19, 20], semiconductor quantum dots (QDs) are arguably the most promising sources of entangled photons [21, 22]. They can generate pairs of photons [23] on demand [15–17], with high photon flux [24–28], high indistinguishability [16, 27, 29], and high entanglement fidelity [30–33], and their emission properties can be tailored by adjusting the growth parameters [34] and/or by the application of external perturbations [35–38]. In the last few years, proof-of-concept experiments, such as quantum teleportation [39, 40], entanglement swapping [41, 42], generation of cluster states [43, 44], and entanglement-based quantum key distribution [45, 46], have demonstrated the potential of QD-based entangled photon sources. Despite these accomplishments, their exploitation in real-life applications is still in its infancy. The main reason is that applications demand the simultaneous optimisation of several different figures of merit of the source. However, to date, each of them requires advanced technological solutions that are often incompatible with each other. To provide an example, let us consider a point-to-point entanglement-based quantum key distribution [47]. For this application, particularly for the implementation of device-independent scenarios [48], it is fundamental to minimize the quantum bit error rate and simultaneously maximize the key rate. Looking at the photon source, this prospect implies simultaneously boosting to near-unity values (*i*) the degree of entanglement and (*ii*) the photon extraction efficiency—a task that is far from easy for QDs, as detailed below.

Concerning (*i*), QDs can generate pairs of polarization-entangled photons via the radiative cascade of a biexciton (XX) to the ground state (0) via the intermediate exciton (X) levels [49]. Experiments have demonstrated that the measured degree of entanglement can be limited by several physical processes, including hyperfine interaction [50], optical Stark effect [51], re-excitation [24], exciton scattering with excess charges [52], and anisotropic electron–hole exchange interaction [53]. After 20 years of research on the subject, a degree of entanglement as high as 0.98 was finally achieved [30], without resorting to inefficient and impractical temporal/spectral post-selection. The key ingredients are the use of GaAs/AlGaAs QD samples with short radiative decay times [54], two-photon resonant excitation [15, 17], and, most importantly, anisotropic strain fields delivered by multi-axial piezoelectric actuators [55, 56]. The latter can be used to cancel any residual fine structure splitting (FSS, with a magnitude s) between the intermediate X states (induced by the anisotropic electron–hole exchange interaction), which leads to the evolution of the entangled state over time, which cannot be fully captured by detectors with finite time resolution. Several external perturbations (such as strain, electric, or magnetic fields [57] or a combination of them) can be used to erase the FSS; our choice is to rely solely on multi-axial strain fields which, until now, is the only method that has demonstrated the capability to achieve a near-unity entanglement degree by erasing the FSS virtually in any QD in the sample.

Concerning (*ii*), embedding a single QD inside an optical cavity [58] is a common strategy adopted to increase the photon extraction efficiency, which is reduced by total internal reflection at the semiconductor-vacuum interface [59]. A cavity allows coupling of the QD emission into the tailored far-field emission pattern of a single mode of the electromagnetic field. This approach also enables the acceleration of spontaneous emission via the Purcell effect [60], opening the path towards GHz operation rates [27]. Over the years, a variety of optical cavities have been used to enhance single optical transitions in QDs [58, 61], with open cavities-systems [62] currently setting the state of the art for single-photon sources. More sophisticated approaches must instead be used for entangled photon sources, mainly because the photons generated in the XX-X-0 cascade features

a difference in energy [63] (a few meV, due to Coulomb interaction among the carriers). Thus, researchers have resorted to photonic molecules [24], nanowires [25], dielectric antennas [26], low-Q micropillars [64], as well as circular Bragg resonators (CBR), or bullseye cavities [65]. In particular, recent works on QDs embedded in CBRs demonstrated extraction efficiencies as high as 0.85(3) [27] with the highest reported entanglement fidelity of 0.90(1) without any reduction of the residual FSS [28].

Previous attempts [66] to combine strain tuning and CBR cavities were limited to the use of monolithic piezoelectric substrates which cannot be used to fully control the in-plane strain anisotropy and are therefore not suitable for the erasure of FSS and the generation of highly entangled photons. Merging the CBRs and multiaxial-strain-tuning technologies would be the ideal choice for applications needing high entanglement degrees such as entanglement-based quantum key distribution. However, this task turned out to be challenging both because of the need to attain tight control over the anisotropy of the strain transferred to the QDs embedded in the CBR cavities and for the additional fabrication steps needed. In this work, we overcome these obstacles and present the first entangled-photon emitter based on a single GaAs/AlGaAs QD, embedded in a CBR, and integrated onto a micromachined piezoelectric actuator that allows for three-axial strain engineering and FSS erasure. This device combines at the same time high brightness, energy tuning, and entanglement optimization.

2 Results

2.1 Sample processing

A sketch of the device discussed in this work is shown in Fig. 1a. The cavity consists of a ~ 670 nm diameter disc with the QD in its geometrical centre, surrounded by a circular Bragg grating made of several trenches with a period that matches the second-order Bragg condition [67] to reflect light travelling inside the semiconductor in the orthogonal direction. The grating, combined with a metallic mirror below the structure, should theoretically result in a quasi-Gaussian emission profile from the top surface. The CBR features a rather flat extraction efficiency profile over tens of nm of wavelength and a low-Q (~ 100) cavity mode enabling modest Purcell enhancement of both the X and XX emission [68–70]. The entire cavity is integrated onto a 300 μm thick $[Pb(Mg_{1/3}Nb_{2/3})O_3]_{0.72}$-$[PbTiO_3]_{0.28}$ (PMN-PT) piezoelectric plate micromachined via femtosecond-laser cut into six actuators ("legs") aligned at 60° to each other. Voltages applied to pairs of aligned legs control three independent strain fields that can be used to tune QDs for the generation of entangled photons with tuneable energy [55]. The integration of the CBR cavity onto the micromachined piezoelectric actuator requires several different technological advances, as discussed in more detail below.

The processing starts with the sample grown on a GaAs(001) substrate in a molecular beam epitaxy (MBE) machine (see Methods for further details). The optically active area consists of a layer of GaAs QDs obtained via the Al-droplet-etching-epitaxy technique [54] placed at the centre of a 140 nm thick $Al_{0.33}Ga_{0.67}As$ layer sandwiched between two 4-nm thick GaAs protective layers. An $Al_{0.75}Ga_{0.25}As$ layer is grown below the active layer to enable substrate removal.

The surface of the sample is coated with a broadband mirror in a two-step deposition process, with a gold film deposited on top of an aluminium oxide layer to avoid potential plasmonic losses at the metal interface [71], as shown in Fig. 1b.

The Au-coated surface is then bonded with a photoresist (SU-8) to a carrier made of a 350 μm thick GaAs substrate by the application of pressure and high temperature (230 °C). The GaAs carrier is thinned by mechanical lapping to a final thickness of less than 50 μm. The thickness of the GaAs carrier must be as low as possible to ensure the largest strain transfer [55] while providing reliable mechanical support to the membrane during all processing steps. The sample with the thinned-down carrier is bonded with SU-8 to the micromachined piezoelectric substrate, as shown in Fig. 1c. The contacts on the piezoelectric substrates allow the application of three independent voltages, as described elsewhere [36]. The original GaAs substrate, together with the sacrificial layer, is removed with a three-step wet etching procedure, as shown in Fig. 1d. The surface of the resulting QD nanomembrane on top of the oxide/Au reflector is spin-coated with an electron-beam resist and patterned using electron beam lithography (EBL) with a square grid of markers. A 150 nm thick stack of equally thick (strain-compensated) Cr-Au-Cr layers is evaporated onto the surface, forming the grid after lift-off. The markers are used as a frame of reference to acquire the positions of single QDs with 15 nm precision in a cryogenic microscopy setup [72], see Fig. 1e. The acquired positions are used to create a pattern of the microcavities with single QDs at their centres in a second EBL step. The patterned cavity designs are transferred onto the semiconductor membrane by dry etching in an inductively coupled plasma machine (Fig. 1f), followed by mask removal (Fig. 1g). Given the narrow emission energy distribution of the QDs, the broadband response of the cavities, and tunability of the final device, the cavity design is adjusted to match the average emission energy of the QD ensemble without adapting the design

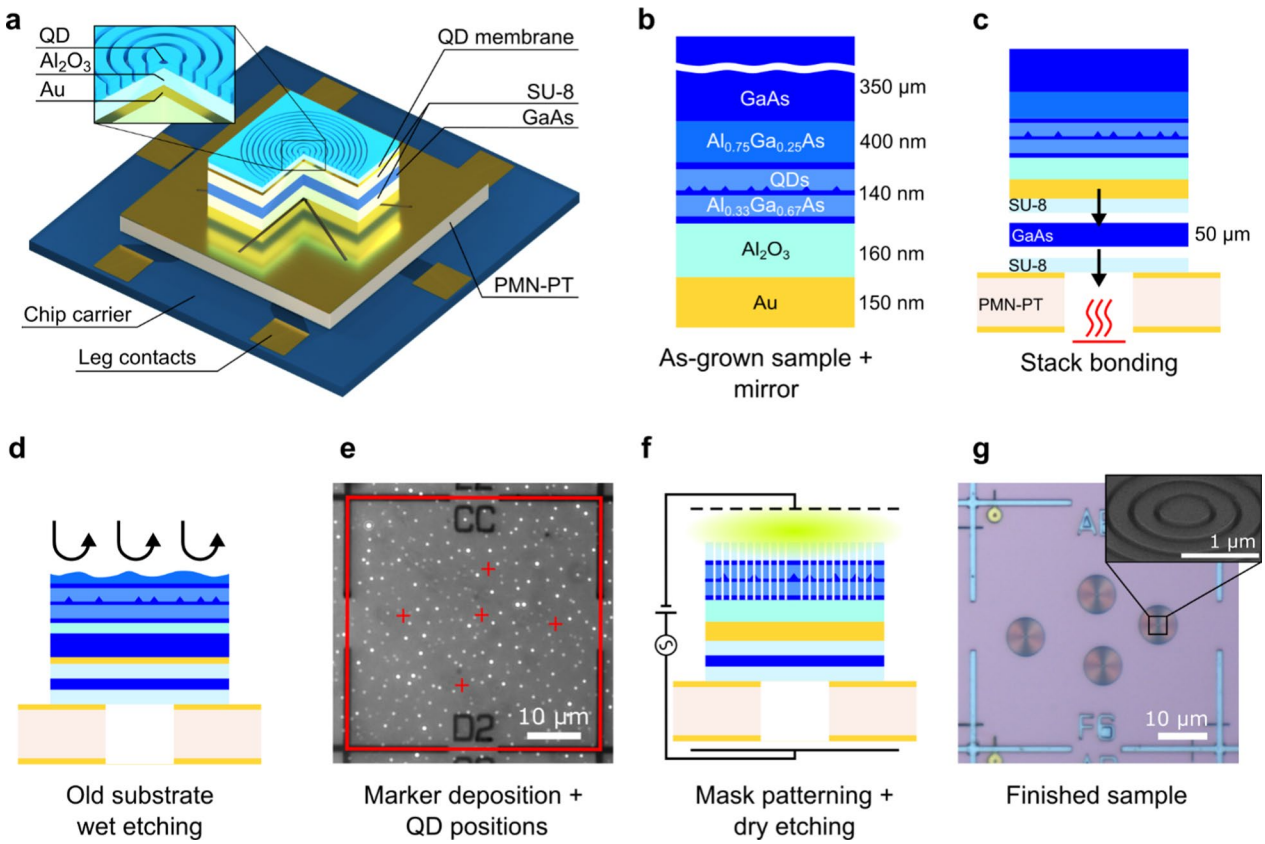

Fig. 1 Processing steps for fabricating a circular Bragg resonator (CBR) cavity on a piezoelectric substrate. **a** Schematic of a CBR sample on six-legged piezoelectric substrate mounted on a chip carrier. Dimensions are not to scale. **b** As-grown quantum dot (QD) sample structure with the oxide and metal mirror deposited on the surface. **c** The sample is bonded with SU-8 photoresist on a GaAs carrier by applying pressure and heat to reach the curing temperature of the photoresist (230 °C). The carrier is later lapped to reduce its thickness to approximately 50 µm. After thinning, the sample is bonded suspended onto the six-legged piezoelectric substrate by using the same procedure. **d** The original substrate and the sacrificial layer are removed via wet etching. **e** Cryogenic optical microscope image showing the photoluminescence of single QDs and a square grid of metallic markers defined on the sample surface via electron beam lithography (EBL) and metal deposition to create a frame of reference. The red square is the result of marker recognition obtained with image processing software. The red crosses represent the positions of single QDs obtained with a 2D Gaussian fit of the QD emission. **f** CBRs are defined in a second EBL step around preselected single QDs. The masked sample is then dry-etched with chlorine and argon plasma in an inductively coupled plasma machine to transfer the cavities onto the membrane. **g** Optical microscopy image of a finished sample. A tilted scanning electron microscope image of the centre of a single structure is shown in the inset

of each cavity to the properties of the embedded emitter. For complete details about all the processing procedures and parameters and the QD position mapping method, see section S1 of the Supplementary Information.

2.2 Optical characterization

Figure 2a shows the low-temperature (5 K) spectra of two exemplary QDs from two different samples excited under resonant two-photon excitation (TPE) [15, 17] with a laser pulse length of 5(1) ps (see Methods). The two QDs emit in the vicinity of the D_1 and D_2 transitions of rubidium (Rb), a possible material choice for the realization of quantum memories [36, 73]. The two most intense lines in the two spectra correspond to the XX and X transitions, as indicated for both the low-energy QD (QD1) and the high-energy QD (QD2). The other lines and the broad band below the XX transitions are likely due to other charged excitonic states [74]. Fine-tuning of the emission energy toward resonance with the Rb transitions can be achieved by applying voltages to one of the legs of the actuator (see the inset of Fig. 1a). The average tuning range achieved for the devices discussed in this work is about 90 neV/V.

To evaluate the acceleration of the spontaneous emission due to the Purcell effect we collect time-resolved emission decay traces. Figure 2b shows the X and XX decay traces under resonant TPE of QD3 which has the highest Purcell factor in the sample, with an X emission

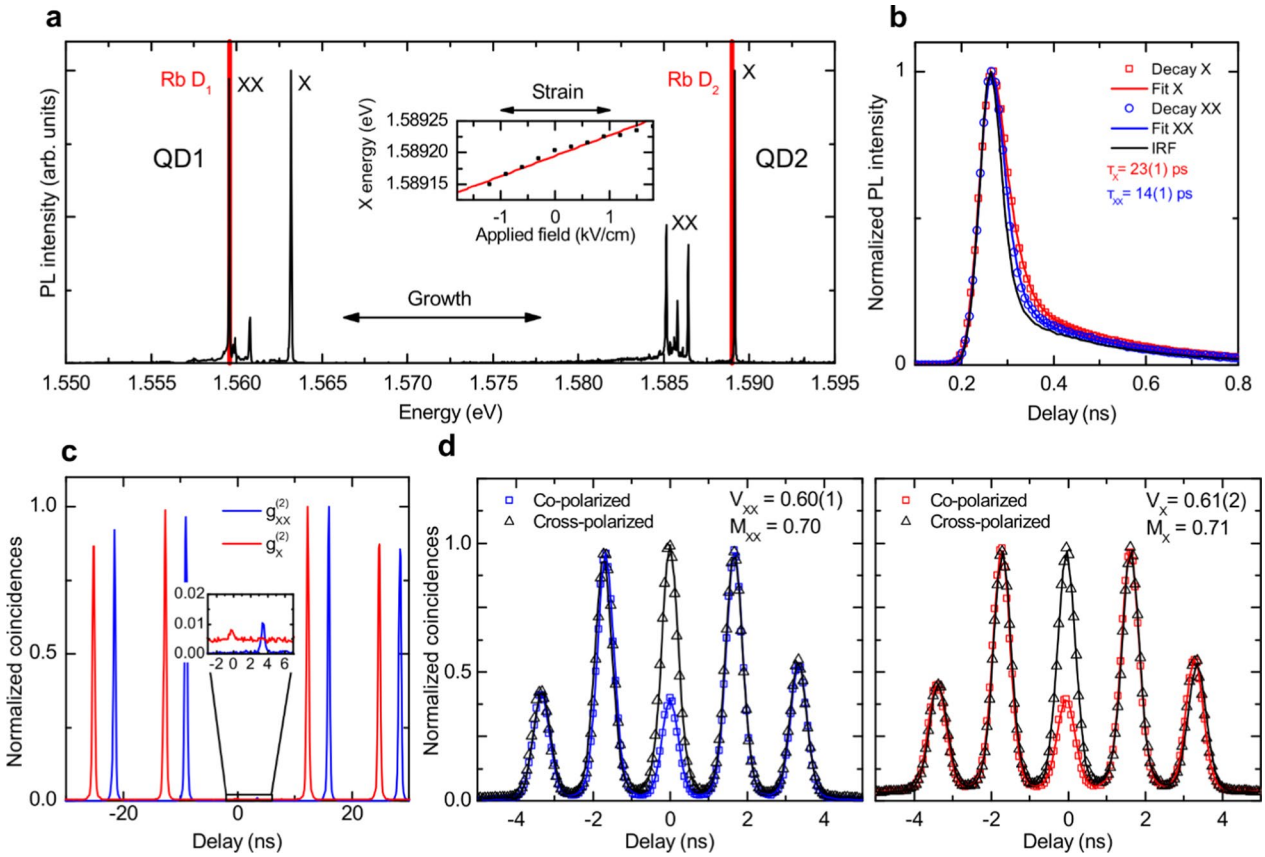

Fig. 2 Optical characterization of cavity-enhanced QDs. **a** Photoluminescence spectra of two representative QDs (labelled QD1 and QD2) from two different samples showing emission in the vicinity of the D_1 and D_2 transitions of rubidium (Rb). The exciton (X) and biexciton (XX) transitions are labelled. The emission of the QD can be tuned toward the resonance of the Rb transitions with the application of stress, as shown in the inset. **b** Time-resolved traces of the X (red squares) and XX (blue circles) transition intensities via resonant two photon excitation (TPE) from the lowest lifetime QD (QD3) in the sample and instrument response function (IRF) (black solid line) of the setup. The lifetime values are obtained with a fit (solid lines) convoluting the IRF with the exponential decay functions expected from the radiative cascade. **c** $g^{(2)}(\tau)$ histograms of the X (red line) and XX (blue line) emission lines for QD2. The histograms are shifted horizontally for ease of reading. The graphs around the 0-time delay are magnified in the inset to highlight the residual low coincidences. The values of the $g^{(2)}(0)$ are $g^{(2)}_{XX}(0) = 0.012(1)$ and $g^{(2)}_{X}(0) = 0.016(1)$. **d** Histograms of Hong-Ou-Mandel interference between co- (red/blue squares) and cross-polarized (black triangles) photons from X and XX decay, respectively, from QD2. The values of the visibility V are obtained using Gaussian peaks convoluted with an exponential decay fit of the peaks (solid lines). The values for the indistinguishability $M_X = 0.71$ and $M_{XX} = 0.70$ are calculated by considering the imperfections of the setup and the values of the $g^{(2)}(0)$, see text for more details

energy of 1.589 eV. A convolution fit of the experimental data with the instrument response function (IRF, black curve) provides lifetimes of 23(1) ps and 14(1) ps for the X and XX transitions, respectively. Considering the measured lifetimes in the bulk sample [41], we calculate a Purcell factor of 11.7(5) and 9.3(5) for X and XX, respectively.

One of the most important properties of a quantum emitter is the ability to emit only a single photon in a given spectral window per excitation pulse. To evaluate the probability of multiphoton emission we perform autocorrelation measurements and estimate the value of the second-order correlation function $g^{(2)}(\tau)$ at $\tau = 0$. For these measurements, the duration of the excitation laser pulse was set to 1.9(3) ps to limit the effect of re-excitation during the same laser pulse [14]. The $g^{(2)}(\tau)$ histograms for QD2 are shown in Fig. 2c for both the X and XX photons, red and blue curves, respectively. The values obtained from the histograms, $g^{(2)}_{XX}(0) = 0.012(1)$ and $g^{(2)}_{X}(0) = 0.016(1)$, are mainly limited by the use of a white halogen lamp to mitigate blinking [75] and by the non-perfect rejection of the resonant laser and/or QD sidebands (see Methods).

The extraction efficiency, i.e., the fraction of photons collected by the lens on top of the samples for the X and XX photons are $\eta_X = 0.67(3)$ and $\eta_{XX} = 0.69(4)$.

For a laser with a repetition rate of 80 MHz, these results in a measured 3.13(1) Mcps and 3.52(1) Mcps at the single photon avalanche photodiodes (SPADs) for the brightest QD in the sample, resulting in 0.155(1) Mcps of measured X-XX coincidences. Considering the efficiency and the nonlinear response (due to the dead time) of the detectors, we estimated an average rate of single photons that arrive at each detector of 9.6(1) Mcps. The pair brightness at the first lens, i.e., the amount of photon pairs that arrive at the first lens of the setup per excitation pulse, is 0.13(1). It is calculated by multiplying the pair emission efficiency $\eta_{pair} = 0.279(3)$, which contains all the effects reducing the pair emission rate, i.e., the preparation fidelity ($\eta_{prep} = 0.96$) and the blinking of the QD ($\eta_{blink} = 0.29$), times both the extraction efficiencies η_X and η_{XX}. For more details on the calculation of the different figures of merit see section S5 of the Supplementary Information.

Another important property of the emitted photons is their indistinguishability, i.e., the degree of similarity between subsequently emitted photons in terms of their different degrees of freedom, such as energy, dispersion, and wavepacket shape. Indistinguishability is fundamental in all applications that need the interference of two photons, e.g., quantum teleportation and entanglement swapping, as the fidelity of the process decreases steeply as the indistinguishability of the two involved photons decreases [76]. To assess the indistinguishability of the X and XX photons, we measure the two-photon interference visibility by exploiting the Hong-Ou-Mandel effect [77] (see Methods). A histogram of the coincidences between the two exit ports of the beam splitter, where photons emitted are allowed to interfere, is shown in Fig. 2d for QD2. The photon states are prepared before interference with both the same and orthogonal polarization. The visibility of the 0-time delay peak can be used to calculate the indistinguishability of the emitted photons [78] and it is obtained from the data with a fit model made by Gaussian functions convoluted with an exponential decay curve. The visibility values obtained from the fit are 0.60(1) and 0.61(2) for the XX and X photons, respectively. It is worth mentioning that these values are obtained without resorting to any spectral or temporal filtering of the photons. By considering the values for the visibility of the interferometer (0.96), the non-zero values of the $g^{(2)}(0)$ (0.025(5) obtained under similar conditions for both X and XX photons), and the non-ideal beam splitter ratio (R = 0.48), we calculate [78] an indistinguishability $M_X = 0.71$ and $M_{XX} = 0.70$. These values are mainly limited by the time-correlations between the two photons emitted during the cascade. The theoretical upper limit [29], which depends on the ratio between the lifetimes of the XX and X, is 0.71(2) for this particular QD, featuring a transition lifetime of 44(3) ps for X and 18(1) ps for XX (see section S3 of the Supporting Information for lifetime data), which is in excellent agreement with the measured values.

2.3 Strain tuning and entanglement recovery

To recover the maximum entanglement degree of the X and XX photons when measuring with detectors with finite time resolution, the FSS of the QD must be reduced to a value much smaller than the natural linewidth of the emission [49]. In the case of Purcell-enhanced emission, the increase of the natural linewidth of the emitted photons (due to the accelerated spontaneous emission rate) strongly relaxes the demand for an ultra-small FSS. As an example, the natural linewidth of the X transition changes from 2.4 μeV for a 270 ps lifetime (typical for QDs in as-grown samples [41]) to 15 μeV for a 40 ps lifetime [49] (i.e., for a Purcell factor of about 7, easily achievable for QDs in our device). Therefore, we expect that QDs featuring large Purcell enhancement will generate entangled photons already at relatively large FSS. To observe this effect, we adjust the voltage applied to the micromachined piezoelectric actuator to restore the in-plane symmetry of the QD confining potential [79] and tune the FSS below the resolution of our set-up, while measuring the entanglement of the emitted photons. As described in previous works [55], this task can be accomplished by sweeping the voltages of one pair of legs for different values of the voltages applied to another pair of legs (the third pair of legs can be used to change the energy of the emitted photons at zero FSS). As shown in Fig. 3a for QD2, this allows us to quickly identify the unique [36] set of electric fields applied to the piezoelectric that allows suppressing the FSS, being $E_{1\text{-}4} = 12$ kV/cm and $E_{2\text{-}5} = 6.67$ kV/cm, see also section S6 of the Supplementary Information. The procedure is better understood by looking at the polarization dependence of the emission energy of the X and XX. The polar plots in Fig. 3b, c report the polarization dependence of the deviation of the X emission from its unperturbed value. The amplitude of the sinusoid is the magnitude of the FSS while the phase gives the polarization direction of the X emission. By applying an electric field on legs 2 and 5 while keeping legs 1 and 4 at 0 kV/cm, we apply stress to the QD (straight arrows) and rotate the polarization axis (curved arrows) until it is aligned with the direction along which the stress is applied by another pair of legs, see the green and the dark orange plots in Fig. 3b, corresponding to the points in Fig. 3a circled with the same colour. After this, we change the electric field on the now aligned legs, e.g., 1 and 4, see the dark orange points in Fig. 3c, until the oscillation of the emission energy goes

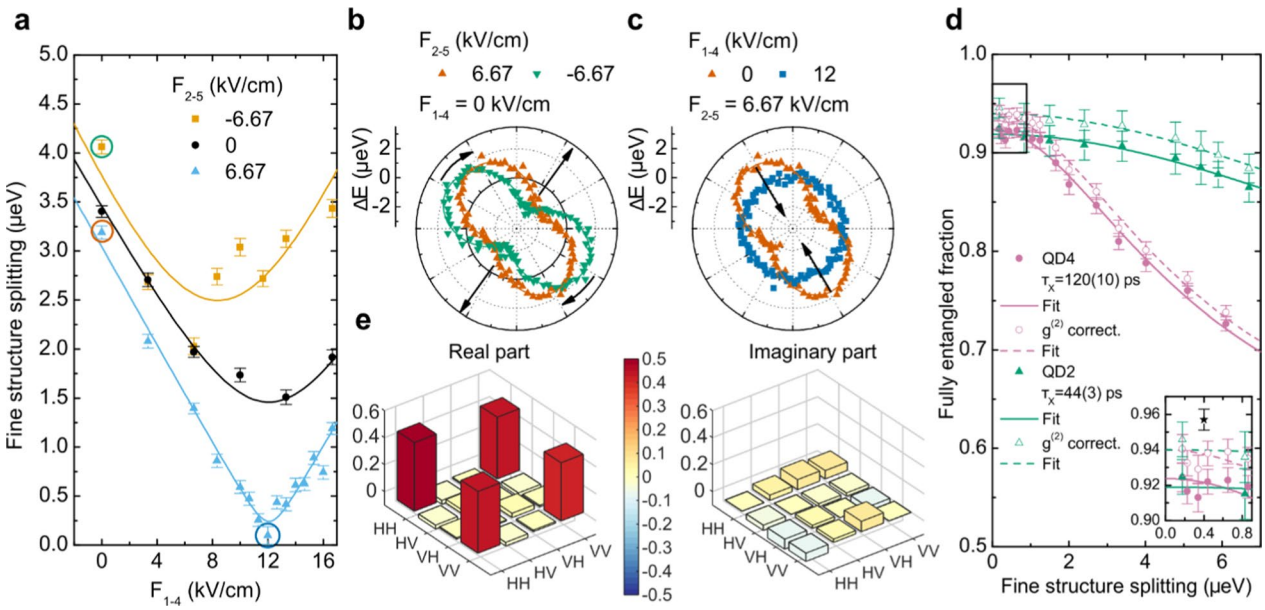

Fig. 3 Entanglement recovery via strain-tuning of the QD. **a** Fine structure splitting (FSS) of the X level for different values of the electric field applied to legs 1and 4 of the piezoelectric device while varying the value of the electric field applied to legs 2 and 5. The solid lines are given as a guide to the eye. The differently coloured circled points correspond to the curves in the polar plots of panels b and c. **b** Polar plot of the distance of the X emission energy from its unperturbed value for two different fields on legs 2 and 5 of the device, while keeping the field value of legs 1 and 4 at 0 kV/cm. The straight arrows highlight the alleged strain direction while the curved arrows highlight the rotation of the polarization angle. **c** Same as b but for different values of the field of legs 1 and 4 of the device, while keeping the value of legs 2 and 5 at 6.67 kV/cm. **d** Fully entangled fraction, namely the maximum fidelity to a maximally entangled state versus the FSS, for the emitted photon pair of QD2 (green triangles) with higher Purcell factor ($\tau_X = 44(3)ps$) and QD4 (pink circles) with lower Purcell factor ($\tau_X = 120(10)ps$). The hollow data points correspond to the same measurements corrected for the non-zero value of the $g^{(2)}(0)$. The solid and dashed lines are fits of the data, raw and $g^{(2)}$-corrected respectively, using a simplified model of the FEF, see text. The black star point in the magnified inset is obtained by reducing the laser pulse length to 1.9(3) ps. **e** Reconstructed density matrix at the highest fully entangled fraction of QD2 of panel (**d**)

to zero, dark blue points in Fig. 3c. In this condition, the emission energy of the QD does not depend anymore on the selected polarization since the degeneracy of the X level is restored, i.e., the FSS is erased, corresponding to the dark blue circled point in Fig. 3a.

To measure the entanglement of the photon pair and gain complete information on its polarization state, we performed a quantum state tomography of the X-XX two-photon state for different decreasing values of the FSS down to zero. By reconstructing the two-photon density matrix, we can estimate the degree of entanglement in terms of the maximal fidelity to a Bell state that can be achieved with simple unitary transformations. This quantity is also known as fully entangled fraction [80] (FEF) and is not affected by possible undesired rotations in the polarization states. It is defined as the overlap between the experimental state $\widehat{\rho}$ and a maximally entangled state $|\Phi\rangle$ maximized over all possible choices of $|\Phi\rangle$: $F = \max_{|\Phi\rangle}\{\langle\Phi|\widehat{\rho}|\Phi\rangle\}$.

The graph in Fig. 3d shows the FEF of the two-photon state versus the FSS for two QDs (QD2 and QD4) featuring two different values of the lifetime for the X transition, i.e., QD2 with 44(3) ps and QD4 with 120(10) ps (the cavity modes and lifetime traces of the two QDs are reported in Figs. S9 and S10 of the Supplementary Information). Both the QDs are excited with a 5(1) ps laser pulse length. As expected, the QD with a shorter (longer) lifetime shows a level of entanglement that varies slowly (rapidly) with the FSS [49]. For the two QDs, we fit the experimental FEF with a simplified model [76]:

$$FEF = \frac{1}{4}\left(1 + k + \frac{2k}{\sqrt{1 + \left(\frac{s\tau_X}{\hbar}\right)^2}}\right)$$

where τ_X is the lifetime of the X state, s is the magnitude of the FSS, and k is a parameter that takes into account decoherence processes and multiphoton emission [49, 76]. The value of the X lifetime obtained for the QD2 curve fit is 51(5) ps which is in good agreement with the measured lifetime of 44(3) ps. The fitted value for QD4 is 164(9) ps, which is significantly larger than the measured one of 120(10) ps. This discrepancy may be related to the presence of other sources of entanglement

degradation such as decoherence, spin and charge noise or other entanglement degrees of freedom not taken into account in the model that might impact a longer lifetime QD more, e.g., a relatively large lifetime means that the system has more time to dephase. The values for k are $k = 0.892(6)$ for QD2 and $k = 0.898(7)$ for QD4. The maximum raw value for the FEF is 0.93(1) and is reached for a FSS of 0.2(2) μeV, see inset of Fig. 3d. The corresponding density matrix is shown in Fig. 3e. We can take into account the effect of the non-zero values of the $g^{(2)}(0)$ in the calculation of the FEF values, by removing the counts stemming from multiphoton emission from the coincidences [81]. The corrected value for the FEF at the same FSS value is 0.95(1) which corresponds to a concurrence of 0.90(2). The $g^{(2)}$-corrected data points for the FEF are plotted in the same graph in Fig. 3d as hollow points and fitted with the same model. As expected, the lifetime values stay the same while the values for the fraction $k = 0.920(6)$ is higher and the same for both QDs.

An improved value for the corrected FEF, i.e., 0.96(1), see star point in the inset of Fig. 3d, is measured after reducing the AC-Stark shift induced by the laser pulse on the X level [51, 82] by decreasing the laser pulse temporal length to 1.9(3) ps.

3 Discussion

To summarize, in this work we demonstrate for the first time a device that combines Purcell-enhanced QDs and a piezoelectric actuator that tunes them for maximizing the degree of polarization entanglement of the emitted photon pairs. More specifically, we show the generation of photon pairs with an entanglement fidelity as high as 0.96(1) and, simultaneously, with an extraction efficiency up to 0.69(4). While these values taken individually do not surpass the best figures of merit that can be found in the literature [27, 28, 30], our work sets the state of the art for a deterministic source of non-classical light that optimizes both brightness and entanglement, see Table 1. This is highly relevant for real-life application in quantum communication, and in particular for entanglement-based quantum key distribution (E-QKD). The successful implementation of an E-QKD protocol depends on the evaluation of the quantum bit error rate (QBER) and the Bell parameter S [83] which both strongly depend on the entanglement fidelity of the photon source used [45]. We believe that the efforts to implement practical quantum technologies are just as complex and important as those that aim at demonstrating the superior performances of one source compared to another. That said, we envisage that further improvements of the device concept we propose here could be used to exceed [84] the key rates achievable with ideal SPDC sources [45, 85] in an E-QKD protocol. A conceptually simple (but technologically challenging) improvement is the integration of a diode-like structure [62, 86] onto the micro-machined piezoelectric actuator. By placing the QDs in the intrinsic region of a *p-i-n* structure [35] and changing the geometry of the photonic structure via small bridges between the CBR rings [87], it is possible to establish electrical connections in the vicinity of the QD. This would allow the application of an electric field across the QDs to counteract possible decoherence mechanisms related to charge noise and thus boost the degree of entanglement to unity values [49]. Moreover, allowing controlled charge tunnelling into/out of the QDs would also enable blinking suppression [88], which would push the flux of entangled photons impinging on the detectors up to a factor of about 3.4 (we estimate 33 Mcps at the single photon detector for the QDs used here), i.e., values close to the record obtained for single photons [62]. Another investigation tool, such as photon correlation Fourier

Table 1 Comparison between the figures of merit of this device and state-of-the-art entangled photon sources for different device architectures

	Extraction efficiency[a]	Multiphoton probability	Indistinguishability	Strain tunability	Entanglement fidelity	Tuning of the FSS
This work	0.69(4)	0.012(1)	0.71(1)	90 neV/V	0.96(1)	Yes
CBRs	0.85(3) [27]	0.001(1) [27]	0.903(3) [27]	–	0.90(1) [28]	No
CBRs on mono. piezo [66]	0.104	0.0015(5)	0.22(2)	1.74 μeV/V	–	No
Planar cavity [3]	0.07 [41]	0.008(2) [32]	0.93(7) [30]	16 μeV/V[b]	0.98(1) [32]	Yes
Broadband antenna [26]	0.65(4)	0.002(2)	–	–	0.90(3)	No
Membrane on chip [37]	–	–	–	120 μeV/V	0.733(75)	Yes
Quantum photonics chip [91]	–	–	–	1.6 μeV/V	0.71(3)	Yes

[a] Single photon

[b] Measured on a 100 nm thin membrane without DBR planar cavity [36]

spectroscopy [89] would help us to have a deeper understanding of the blinking dynamics and line broadening of the QD emission. The Purcell enhancement plays a major role in relaxing the demand for low FSS. By looking at Fig. 3d, the shorter lifetime QD (green curve) exhibits a corrected fidelity above 0.90 for up to 4 μeV of FSS while at the same time showing an emission energy shift of approximately 40 μeV (0.02 nm). The reduced tuning range shown in this sample is arguably due to the 50 μm thick GaAs carrier introduced to increase the stiffness of the membrane. This is confirmed by the fact that in CBRs structures on a monolithic piezoelectric [66] the achieved tuning range is 1.74 μeV/V, see Table 1, but with a 30 μm thick GaAs carrier. Moreover, previous works [36] using a 100 nm thick semiconductor membrane with no GaAs carrier show a tuning range which is more than two orders of magnitude higher (16 μeV/V) than the one achieved in this work against a simulated maximum range of 160 μeV/V [55]. Getting tuning ranges closer to these values could be achieved by thinning down the GaAs carrier to a thickness in the order of hundreds of nm at the cost of introducing the technological challenge of providing mechanically stable membranes capable of enduring all the processing steps involved. We can, however, make more quantitative calculations on the advantage of having a reduced amount of tuning compared to no tuning at all. If we consider the energy distribution of the QD emission energy in these samples (a normal distribution with 5 meV of standard deviation), the probability of finding a QD which has an emission energy within a distance equal to 1% of its linewidth from a specific line, e.g. the Rb absorption, is around 1 to 100′000. With a 90neV/V tuning range, considering the maximum voltage range sustainable by the piezoelectric substrates (up to ± 600 V), the amount of QDs that can be tuned in resonance with a specific line is ~ 1%, with an improvement of almost 3 orders of magnitude.

Further refinements of the device concept would also enable the use of QDs in other quantum communication applications that need indistinguishable photons, such as entanglement swapping, quantum repeaters, and in general, multi-node quantum networks. These protocols will require levels of indistinguishability beyond the 70% demonstrated in this work. While the use of an electric field will certainly help in stabilizing the charge environment and reduce spectral wandering [90], boosting the indistinguishability to near unity values requires overcoming the time-correlation between the photon pairs generated during the biexciton cascade. A possible solution to alleviate this hurdle would be the use of a cavity that exploits the Purcell effect to engineer the ratio between the X and XX lifetime [29]. For example, a ratio of 3, a value that can be easily reached in our current device structure, would result in a theoretical photon indistinguishability of up to 0.86. Larger values could be in principle achieved by improving the cavity quality factor while keeping the same broadband extraction efficiency [27]. All these steps will certainly require additional technological advances. However, the efforts are justified as the development of a deterministic source of entangled photons that optimize brightness, degree of entanglement, and indistinguishability would mark the departure from a pioneering phase that is lasting for more than 20 years and would finally open the path towards the exploitation of QDs in real-world applications.

4 Methods

4.1 Semiconductor QD sample structure

A sacrificial layer of $Al_{0.75}Ga_{0.25}As$ is first grown on a 350 μm thick GaAs (001) commercial substrate in a MBE system. Then, the membrane containing the QDs is grown by first depositing a 4 nm thick layer of GaAs to protect the AlGaAs matrix from oxidation, followed by a first 69 nm thick layer of $Al_{0.33}Ga_{0.67}As$. The QDs are obtained by evaporating Al on the surface to form droplets drilling highly symmetric nanoholes on the surface [54]. The holes are then filled with a 1.5 nm thick layer of GaAs and capped with another 70 nm thick layer of $Al_{0.33}Ga_{0.67}As$ for a total thickness of the membrane of roughly 140 nm. The structure is then protected with another 4 nm thick layer of GaAs bringing the total thickness to 148 nm.

4.2 Cryogenic microscope setup

To record the positions of QDs for the deterministic fabrication of the CBRs we employ cryogenic imaging using two light sources simultaneously. A blue light emitting diode (LED) (central wavelength of 470 nm) excites QDs above-band gap while an infrared (IR) LED (central wavelength of 810 nm) illuminates the sample located in a liquid-He continuous-flow cryostat, optically accessed using a 0.85 NA glass-corrected objective through a 200 μm thick window. An image of the spatially resolved PL signal and the reference markers is formed on a cost-effective CMOS camera. High-resolution images are acquired with low gain and an exposure time of 1 s and are numerically processed with a Python script that fits the reference markers with straight lines and the QD emission spots with 2D-Gaussian functions. The size of QD spots in the image is close to the diffraction limit. Repeating the detection process of single QDs in 30 different images of the same marker field yields statistical information on the position accuracy, with the most common value for the standard deviation below 15 nm. A more detailed description of the cryogenic imaging setup

and the numerical methods is provided in section S1 of the Supplementary Information.

4.3 Photoluminescence setup

The processed sample is mounted on a sample holder and the six legs of the micromachined piezoelectric substrate are contacted with Manganin wires. The sample holder is thermally connected to the cold finger of a closed cycle He cryostat which is equipped with electrical feedthroughs for the application of high voltages to the micromachined piezoelectric actuator. A 0.5 NA aspheric lens is used to focus the laser light and collect the photoluminescence (PL) signal. The sample is cooled down to 5 K and is excited with a mode-locked pulsed Ti:Sapphire laser. The 140 fs long laser pulses are narrowed in energy with a 4-f pulse slicer to 5(1) ps temporal width. The pulse slicer also allows for the fine-tuning of the central wavelength of the pulse and changing the laser temporal pulse width down to 1.9(3) ps. The QD is excited with a TPE scheme [15, 17] where the laser energy is tuned to half the energy difference of the ground state-XX transition. In this way, the QD is resonantly excited directly to the XX state by absorbing two photons from the laser. A white halogen lamp is focused on the QD to neutralize the charge environment and allow for TPE [75]. The laser signal reflected from the sample is filtered with a set of three volume Bragg grating filters. The PL signal emitted by the QD is analysed with a 750 mm spectrometer equipped with 300, 1200, and 1800 g/mm gratings and a liquid-nitrogen-cooled CCD camera.

4.4 Fine structure splitting measurement

The FSS of the X state is measured by placing in the path to the spectrometer a half-wave plate (HWP) and a linear polarizer. The polarization-resolved spectra of the QD emission are collected at each step of the rotation of the HWP using the 1800 g/mm grating. The half-amplitude of a sinusoidal fit of the energy difference between the X and XX line returns the magnitude of the FSS of the X level with sub-μeV accuracy [92].

4.5 Lifetime measurements

The X and XX emission lines of the QD are selected with the 300 g/mm grating of the spectrometer and the signal is sent to a low-time jitter (70 ps FWHM) SPAD. The signal of the SPAD is sent to a time correlator with a time jitter of 8 ps. Here, a start-stop histogram is created using the TTL signal from a photodiode inside the laser head as a time reference. The instrument response function is obtained by sending the 5(1) ps long laser pulse along the same path. To extract the values of the lifetimes, we perform a fit [93] by the convolution of the IRF with the exponential decay expected from a simple rate equation model of the radiative cascade. For the XX decay, a single exponential is used for the fit, while for the X decay, the fit is done with an exponential decay preceded by an exponential rise with a lifetime equal to the XX decay time. The error on the lifetime is given by computing the χ^2 surface and taking the confidence interval enclosed in a 5% increase of the χ^2.

4.6 Second-order correlation measurements

The signal coming from either the X or the XX transition is separated from the beam path with a volume Bragg grating mirror and sent to a Hanbury-Brown and Twiss [94] setup. Here, a 50:50 fibre beam splitter sends the incoming photons to two SPADs with a time jitter of about 350 ps. The signal from the SPADs is sent to the time correlator that creates a histogram of the coincidences from the two detectors. The values for the $g^{(2)}(0)$ are calculated by normalizing the counts at the 0-time delay to the counts of the side peaks corresponding to consecutive laser pulses.

4.7 Hong-Ou-Mandel interference visibility

To make photons from two consecutive laser pulses interfere, the pulses of the laser are first doubled with an unbalanced Mach–Zehnder interferometer built with a 1.8 ns time difference between the two arms. The same delay difference is then introduced between the arms of a second Mach–Zehnder interferometer in the path of the PL signal. The histogram of the coincidences is collected from the acquisition events of two SPADs at the exit ports of the last fibre beam splitter. The polarization of the photons impinging on the second beam splitter is selected with a linear polarizer and adjusted with a three-pad fibre polarization manual controller on each input arm of the fibre beam splitter.

4.8 2-photon density matrix reconstruction

The density matrix is reconstructed by performing polarization-dependent cross-correlation measurements [95–97] between X and XX photons coupled into single-mode fibres. The matrix is reconstructed from a set of 36 measurements associated with different combinations of polarization bases and using a maximum likelihood method. The error bars on each point of the fidelity are obtained with a Monte Carlo simulation consisting

of 2000 runs, assuming a Poissonian error on the coincidence counts.

Supplementary Information

The online version contains supplementary material available at https://doi.org/10.1186/s43593-024-00072-8.

Supplementary material 1.

Acknowledgements
The authors thank B. U. Lehner, T. Oberleitner, and C. Schimpf for fruitful discussions, as well as U. Kainz, A. Halilovic and A. Schwarz from JKU, A. Miriametro from Sapienza University of Rome, and S. Kuhn from University of Würzburg for technical assistance.

Author contributions
MBR, TMK, and FBB wrote the manuscript with the help of all authors. MBR and TMK developed the fabrication process of the membrane, the cryogenic optical microscope for the quantum dot positioning with the help of GP, XY, and JF. CK wrote the code for cryogenic image processing. QB, MMD, CS, and SH processed the positioned cavities. MBR, TMK, MB, JN, HH, NH, MJ, and GL performed the quantum optical characterization of the samples. MBR analysed the results with the help of MB, HH, and FBB. SFCdS grew the samples with the help of SM. SM performed the simulations of the cavities. SS fabricated the piezoelectric actuators. THL, AR, and RT coordinated the project. All the authors participated in the discussion of the results.

Funding
RT acknowledges the European Research Council (ERC) under the European Union's Horizon 2020 Research and Innovation Program under Grant Agreement No. 679183 (SPQRel), and the MUR (Ministero dell'Università e della Ricerca) through the PNRR MUR Project PE0000023-NQSTI and via the Project PRIN 2017 Taming complexity via Quantum Strategies a Hybrid Integrated Photonic approach (QUSHIP) Id. 2017SRNBRK. RT and AR acknowledge the European Union's Horizon 2020 Research and Innovation Program under Grant Agreement No. 899814 (Qurope), the QuantERA II Programme that has received funding from the European Union's Horizon 2020 Research and Innovation Programme under Grant Agreement No. 101017733 via the project QD-E-QKD and the FFG (Grant No. 891366). RT, AR, and CS acknowledges the European Union's Horizon 2020 (2014–2020) under Grant Agreement No. 731473 (QuantERA project HYPER-U-P-S No. 8C18002). AR also acknowledges the European Union's Horizon 2020 Research and Innovation Program under Grant Agreements No. 871130 (Ascent+), the Austrian Science Fund (FWF) via the Research Group FG5, P 29603, I 4380, I 3762, the Linz Institute of Technology (LIT), and the LIT Secure and Correct Systems Lab, supported by the State of Upper Austria. THL acknowledges funding from the Federal Ministry of Education and Research (BMBF) through the Quantum Futur (FKZ: 13N16272) initiative. MJ acknowledges the Czech Science Foundation (Grant No. 21-18545S). NH acknowledges the European Union's 2020 research and innovation program (CSA-Coordination and support action, H2020-WIDESPREAD-2020-5) under Grant Agreement No. 951737 (NONGAUSS) and under Grant Agreement No. 101017733 via the project QD-E-QKD, and Palacky University (Grants No. IGA-PrF-2022-005, IGA-PrF-2023-006). XY acknowledges support from the National Natural Science Foundation of China (NSFC 12104090), "the Fundamental Research Funds for the Central Universities" and "Zhishan" Scholars Programs of Southeast University.

Availability of data and materials
All data and materials that support the results of this work are available from the corresponding authors upon reasonable request.

Declarations

Competing interests
The authors declare no competing financial or non-financial interests.

Received: 30 April 2024 Revised: 10 June 2024 Accepted: 17 June 2024
Published online: 24 July 2024

References

1. D. Awschalom et al., Development of Quantum Interconnects (QuICs) for next-generation information technologies. PRX Quantum **2**, 017002 (2021)
2. D.A. Vajner, L. Rickert, T. Gao, K. Kaymazlar, T. Heindel, Quantum communication using semiconductor quantum dots. Adv. Quantum Technol. **5**, 2100116 (2022)
3. C.-Y. Lu, J.-W. Pan, Quantum-dot single-photon sources for the quantum internet. Nat. Nanotechnol. **16**, 1294–1296 (2021)
4. E. Pelucchi et al., The potential and global outlook of integrated photonics for quantum technologies. Nat. Rev. Phys. **4**, 194–208 (2021)
5. R. Uppu, L. Midolo, X. Zhou, J. Carolan, P. Lodahl, Quantum-dot-based deterministic photon–emitter interfaces for scalable photonic quantum technology. Nat. Nanotechnol. **16**, 1308–1317 (2021)
6. S. Wehner, D. Elkouss, R. Hanson, Quantum internet: a vision for the road ahead. Science **362**, 9288 (2018)
7. J.-W. Pan et al., Multiphoton entanglement and interferometry. Rev. Mod. Phys. **84**, 777–838 (2012)
8. F. Flamini, N. Spagnolo, F. Sciarrino, Photonic quantum information processing: a review. Rep. Prog. Phys. **82**, 016001 (2019)
9. H.-S. Zhong et al., 12-Photon entanglement and scalable scattershot boson sampling with optimal entangled-photon pairs from parametric down-conversion. Phys. Rev. Lett. **121**, 250505 (2018)
10. S. Meraner et al., Approaching the Tsirelson bound with a Sagnac source of polarization-entangled photons. SciPost Phys. **10**, 017 (2021)
11. M. Takeoka, R.-B. Jin, M. Sasaki, Full analysis of multi-photon pair effects in spontaneous parametric down conversion based photonic quantum information processing. New J. Phys. **17**, 043030 (2015)
12. K.D. Jöns et al., Bright nanoscale source of deterministic entangled photon pairs violating Bell's inequality. Sci. Rep. **7**, 1700 (2017)
13. L. Schweickert et al., On-demand generation of background-free single photons from a solid-state source. Appl. Phys. Lett. **112**, 093106 (2018)
14. L. Hanschke et al., Quantum dot single-photon sources with ultra-low multi-photon probability. Npj Quantum Inf. **4**, 43 (2018)
15. H. Jayakumar et al., Deterministic photon pairs and coherent optical control of a single quantum dot. Phys. Rev. Lett. **110**, 135505 (2013)
16. Y.-M. He et al., On-demand semiconductor single-photon source with near-unity indistinguishability. Nat. Nanotechnol. **8**, 213–217 (2013)
17. M. Müller, S. Bounouar, K.D. Jöns, M. Glässl, P. Michler, On-demand generation of indistinguishable polarization-entangled photon pairs. Nat. Photonics **8**, 224–228 (2014)
18. I. Aharonovich, E. Neu, Diamond nanophotonics. Adv. Opt. Mater. **2**, 911–928 (2014)
19. M. Turunen et al., Quantum photonics with layered 2D materials. Nat. Rev. Phys. **4**, 219–236 (2022)
20. Drawer, J.-C. et al. Monolayer-based single-photon source in a liquid-helium-free open cavity featuring 65% brightness and quantum Coherence. Nano Lett. **23**, 8683–8689 (2023).
21. P. Lodahl, Quantum-dot based photonic quantum networks. Quantum Sci. Technol. **3**, 013001 (2018)
22. C. Schimpf et al., Quantum dots as potential sources of strongly entangled photons: perspectives and challenges for applications in quantum networks. Appl. Phys. Lett. **118**, 100502 (2021)
23. N. Akopian et al., Entangled photon pairs from semiconductor quantum dots. Phys. Rev. Lett. **96**, 130501 (2006)
24. A. Dousse et al., Ultrabright source of entangled photon pairs. Nature **466**, 217–220 (2010)
25. M.A.M. Versteegh et al., Observation of strongly entangled photon pairs from a nanowire quantum dot. Nat. Commun. **5**, 5298 (2014)
26. Y. Chen, M. Zopf, R. Keil, F. Ding, O.G. Schmidt, Highly-efficient extraction of entangled photons from quantum dots using a broadband optical antenna. Nat. Commun. **9**, 2994 (2018)
27. J. Liu et al., A solid-state source of strongly entangled photon pairs with high brightness and indistinguishability. Nat. Nanotechnol. **14**, 586–593 (2019)

28. H. Wang et al., On-demand semiconductor source of entangled photons which simultaneously has high fidelity, efficiency, and indistinguishability. Phys. Rev. Lett. **122**, 113602 (2019)
29. E. Schöll et al., Crux of using the cascaded emission of a three-level quantum ladder system to generate indistinguishable photons. Phys. Rev. Lett. **125**, 233605 (2020)
30. D. Huber et al., Highly indistinguishable and strongly entangled photons from symmetric GaAs quantum dots. Nat. Commun. **8**, 15506 (2017)
31. J. Huwer et al., Quantum-dot-based telecommunication-wavelength quantum relay. Phys. Rev. Appl. **8**, 024007 (2017)
32. D. Huber et al., Strain-tunable gaas quantum dot: a nearly dephasing-free source of entangled photon pairs on demand. Phys. Rev. Lett. **121**, 033902 (2018)
33. C. Hopfmann et al., Maximally entangled and gigahertz-clocked on-demand photon pair source. Phys. Rev. B **103**, 075413 (2021)
34. M. Gurioli, Z. Wang, A. Rastelli, T. Kuroda, S. Sanguinetti, Droplet epitaxy of semiconductor nanostructures for quantum photonic devices. Nat. Mater. **18**, 799–810 (2019)
35. R. Trotta et al., Nanomembrane quantum-light-emitting diodes integrated onto piezoelectric actuators. Adv. Mater. **24**, 2668–2672 (2012)
36. R. Trotta et al., Wavelength-tunable sources of entangled photons interfaced with atomic vapours. Nat. Commun. **7**, 10375 (2016)
37. Y. Chen et al., Wavelength-tunable entangled photons from silicon-integrated III–V quantum dots. Nat. Commun. **7**, 10387 (2016)
38. W. Ou et al., Strain tuning self-assembled quantum dots for energy-tunable entangled-photon sources using a photolithographically fabricated microelectromechanical system. ACS Photonics **9**, 3421–3428 (2022)
39. M. Reindl et al., All-photonic quantum teleportation using on-demand solid-state quantum emitters. Sci. Adv. **4**, eaau1255 (2018)
40. J. Nilsson et al., Quantum teleportation using a light-emitting diode. Nat. Photonics **7**, 311–315 (2013)
41. F. Basso Basset et al., Entanglement swapping with photons generated on demand by a quantum dot. Phys. Rev. Lett. **123**, 160501 (2019)
42. M. Zopf et al., Entanglement swapping with semiconductor-generated photons violates bell's inequality. Phys. Rev. Lett. **123**, 160502 (2019)
43. I. Schwartz et al., Deterministic generation of a cluster state of entangled photons. Science **354**, 434–437 (2016)
44. D. Cogan, Z.-E. Su, O. Kenneth, D. Gershoni, Deterministic generation of indistinguishable photons in a cluster state. Nat. Photonics **17**, 324–329 (2023)
45. F. Basso Basset et al., Quantum key distribution with entangled photons generated on demand by a quantum dot. Sci. Adv. **7**, eabe6379 (2021)
46. C. Schimpf et al., Quantum cryptography with highly entangled photons from semiconductor quantum dots. Sci. Adv. **7**, eabe8905 (2021)
47. R. Ursin et al., Entanglement-based quantum communication over 144 km. Nat. Phys. **3**, 481–486 (2007)
48. A. Acín et al., Device-independent security of quantum cryptography against collective attacks. Phys. Rev. Lett. **98**, 230501 (2007)
49. A.J. Hudson et al., Coherence of an entangled exciton-photon state. Phys. Rev. Lett. **99**, 266802 (2007)
50. C. Schimpf et al., Hyperfine interaction limits polarization entanglement of photons from semiconductor quantum dots. Phys. Rev. B **108**, L081405 (2023)
51. F. Basso Basset et al., Signatures of the optical Stark effect on entangled photon pairs from resonantly-pumped quantum dots. Phys. Rev. Lett. **131**, 166901 (2023).
52. A. Fognini et al., Dephasing free photon entanglement with a quantum dot. ACS Photonics **6**, 1656–1663 (2019)
53. M. Bayer et al., Electron and hole g factors and exchange interaction from studies of the exciton fine structure in In 0.60 Ga 0.40 as quantum dots. Phys. Rev. Lett. **82**, 1748–1751 (1999)
54. Y.H. Huo, A. Rastelli, O.G. Schmidt, Ultra-small excitonic fine structure splitting in highly symmetric quantum dots on GaAs (001) substrate. Appl. Phys. Lett. **102**, 152105 (2013)
55. R. Trotta, J. Martín-Sánchez, I. Daruka, C. Ortix, A. Rastelli, Energy-tunable sources of entangled photons: a viable concept for solid-state-based quantum relays. Phys. Rev. Lett. **114**, 150502 (2015)
56. J. Wang, M. Gong, G.-C. Guo, L. He, Towards scalable entangled photon sources with self-assembled InAs/GaAs quantum dots. Phys. Rev. Lett. **115**, 067401 (2015)
57. R. Trotta et al., Universal recovery of the energy-level degeneracy of bright excitons in InGaAs quantum dots without a structure symmetry. Phys. Rev. Lett. **109**, 147401 (2012)
58. P. Senellart, G. Solomon, A. White, High-performance semiconductor quantum-dot single-photon sources. Nat. Nanotechnol. **12**, 1026–1039 (2017)
59. Y. Ma, P.E. Kremer, B.D. Gerardot, Efficient photon extraction from a quantum dot in a broad-band planar cavity antenna. J. Appl. Phys. **115**, 023106 (2014)
60. E.M. Purcell, H.C. Torrey, R.V. Pound, Resonance absorption by nuclear magnetic moments in a solid. Phys. Rev. **69**, 37–38 (1946)
61. J. Yang et al., Tunable quantum dots in monolithic Fabry-Perot microcavities for high-performance single-photon sources. Light Sci. Appl. **13**, 33 (2024)
62. N. Tomm et al., A bright and fast source of coherent single photons. Nat. Nanotechnol. **16**, 399–403 (2021)
63. A. Schliwa, M. Winkelnkemper, D. Bimberg, Few-particle energies versus geometry and composition of In x Ga 1−x As / GaAs self-organized quantum dots. Phys. Rev. B **79**, 075443 (2009)
64. L. Ginés et al., High extraction efficiency source of photon pairs based on a quantum dot embedded in a broadband micropillar cavity. Phys. Rev. Lett. **129**, 033601 (2022)
65. M.Y. Su, R.P. Mirin, Enhanced light extraction from circular Bragg grating coupled microcavities. Appl. Phys. Lett. **89**, 033105 (2006)
66. M. Moczała-Dusanowska et al., Strain-tunable single-photon source based on a circular bragg grating cavity with embedded quantum dots. ACS Photonics **7**, 3474–3480 (2020)
67. A. Hardy, D.F. Welch, W. Streifer, Analysis of second-order gratings. IEEE J. Quantum Electron. **25**, 2096–2105 (1989)
68. M. Davanço, M.T. Rakher, D. Schuh, A. Badolato, K. Srinivasan, A circular dielectric grating for vertical extraction of single quantum dot emission. Appl. Phys. Lett. **99**, 041102 (2011)
69. L. Rickert, T. Kupko, S. Rodt, S. Reitzenstein, T. Heindel, Optimized designs for telecom-wavelength quantum light sources based on hybrid circular Bragg gratings. Opt. Express **27**, 36824 (2019)
70. S. Kolatschek et al., Bright purcell enhanced single-photon source in the telecom O-band based on a quantum dot in a circular Bragg grating. Nano Lett. **21**, 7740–7745 (2021)
71. H. Galal, M. Agio, Highly efficient light extraction and directional emission from large refractive-index materials with a planar Yagi-Uda antenna. Opt. Mater. Express **7**, 1634 (2017)
72. J. Liu et al., Cryogenic photoluminescence imaging system for nanoscale positioning of single quantum emitters. Rev. Sci. Instrum. **88**, 023116 (2017)
73. H. Huang et al., Electrically-pumped wavelength-tunable GaAs quantum dots interfaced with rubidium atoms. ACS Photonics **4**, 868–872 (2017)
74. D. Huber et al., Single-particle-picture breakdown in laterally weakly confining GaAs quantum dots. Phys. Rev. B **100**, 235425 (2019)
75. T. Huber, A. Predojević, G.S. Solomon, G. Weihs, Effects of photo-neutralization on the emission properties of quantum dots. Opt. Express **24**, 21794 (2016)
76. M.B. Rota, F.B. Basset, D. Tedeschi, R. Trotta, Entanglement teleportation with photons from quantum dots: toward a solid-state based quantum network. IEEE J. Sel. Top. Quantum Electron. **26**, 1–16 (2020)
77. C.K. Hong, Z.Y. Ou, L. Mandel, Measurement of subpicosecond time intervals between two photons by interference. Phys. Rev. Lett. **59**, 2044–2046 (1987)
78. N. Somaschi et al., Near-optimal single-photon sources in the solid state. Nat. Photonics **10**, 340–345 (2016)
79. R. Trotta, A. Rastelli, Engineering of quantum dot photon sources via electro-elastic fields, in *Engineering the atom-photon interaction*. ed. by A. Predojević, M.W. Mitchell (Springer International Publishing, Cham, 2015), pp.277–302
80. J. Grondalski, D.M. Etlinger, D.F.V. James, The fully entangled fraction as an inclusive measure of entanglement applications. Phys. Lett. A **300**, 573–580 (2002)
81. J. Neuwirth et al., Multipair-free source of entangled photons in the solid state. Phys. Rev. B **106**, L241402 (2022)
82. T. Seidelmann et al., Two-photon excitation sets limit to entangled photon pair generation from quantum emitters. Phys. Rev. Lett. **129**, 193604 (2022)

83. J.F. Clauser, M.A. Horne, A. Shimony, R.A. Holt, Proposed experiment to test local hidden-variable theories. Phys. Rev. Lett. **23**, 880–884 (1969)
84. A. Acín, S. Massar, S. Pironio, Efficient quantum key distribution secure against no-signalling eavesdroppers. New J. Phys. **8**, 126–126 (2006)
85. R. Hošák, I. Straka, A. Predojević, R. Filip, M. Ježek, Effect of source statistics on utilizing photon entanglement in quantum key distribution. Phys. Rev. A **103**, 042411 (2021)
86. C.L. Salter et al., An entangled-light-emitting diode. Nature **465**, 594–597 (2010)
87. Q. Buchinger, S. Betzold, S. Höfling, T. Huber-Loyola, Optical properties of circular Bragg gratings with labyrinth geometry to enable electrical contacts. Appl. Phys. Lett. **122**, 111110 (2023)
88. C. Schimpf, S. Manna, S.F. Covre da Silva, M. Aigner, A. Rastelli, Entanglement-based quantum key distribution with a blinking-free quantum dot operated at a temperature up to 20 K. Adv. Photonics **3**, 065001 (2021)
89. C. Schimpf et al., Resolving the temporal evolution of line broadening in single quantum emitters. Opt. Express **27**, 35290 (2019)
90. F. Troiani, Entanglement swapping with energy-polarization-entangled photons from quantum dot cascade decay. Phys. Rev. B **90**, 245419 (2014)
91. T. Jin et al., Generation of polarization-entangled photons from self-assembled quantum dots in a hybrid quantum photonic chip. Nano Lett. **22**, 586–593 (2022)
92. R.J. Young et al., Bell-inequality violation with a triggered photon-pair source. Phys. Rev. Lett. **102**, 030406 (2009)
93. Preus, S. DecayFit - Fluorescence Decay Analysis Software 1.4, FluorTools, www.fluortools.com. FluorTools (2023).
94. R. Hanbury Brown, R.Q. Twiss, A test of a new type of stellar interferometer on sirius. Nature **178**, 1046–1048 (1956)
95. M. Ježek, J. Fiurášek, Z. Hradil, Quantum inference of states and processes. Phys. Rev. A **68**, 012305 (2003)
96. Z. Hradil, J. Řeháček, J. Fiurášek, M. Ježek, 3 maximum-likelihood methods in quantum mechanics, in *Quantum state estimation*. ed. by M. Paris, J. Řeháček (Springer, Berlin, 2004), pp.59–112
97. J.B. Altepeter et al., Experimental methods for detecting entanglement. Phys. Rev. Lett. **95**, 033601 (2005)

Supplementary Information to
A source of entangled photons based on a cavity-enhanced and strain-tuned GaAs quantum dot

S1 | Device Fabrication

Simulations of the cavity

A finite difference time domain (FDTD) based commercial software solution is used to simulate the performance of circular Bragg resonators (CBRs). The performance of Al_2O_3 as a material system for the oxide in the broadband back reflector was studied, with the results in extraction efficiency and Purcell factor provided in Fig. S1.

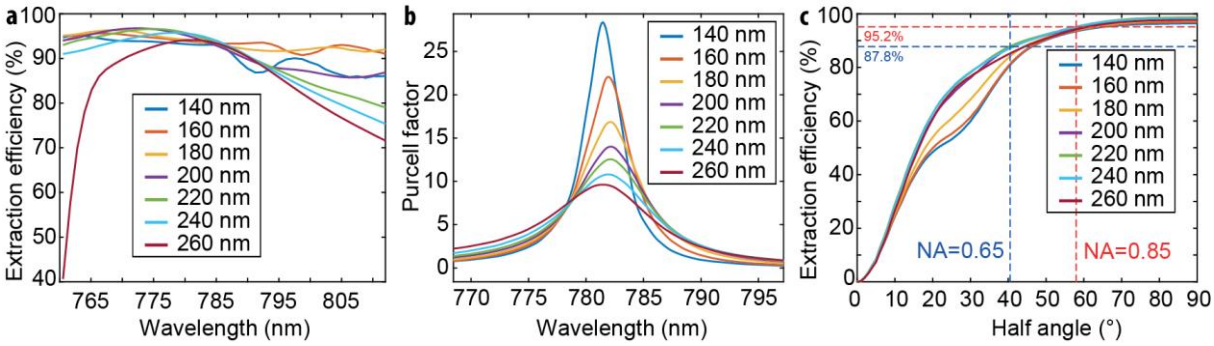

Figure S1 | FDTD simulated data for various Al_2O_3 layer thicknesses (indicated in (a) and (c)) showing **(a)** the extraction efficiency and **(b)** the Purcell factor as a function of wavelength. **(c)** A Gaussian intensity distribution is indicated by a slowly varying extraction efficiency at high collection angles.

Deposition of the back reflector

We employ an atomic layer deposited (ALD) thin film of amorphous Al_2O_3 with a refractive index n = 1.64 at a wavelength of 780 nm that has a nominal thickness of 160 nm. This value is chosen to optimize the performance of the structure, as evaluated via finite-difference time-domain numerical simulations (see Section S1). The layer is grown on a sample with GaAs QDs on a GaAs substrate at a temperature of 200 °C in 1600 cycles, which consist of alternate pulses of trimethylaluminum (TMA) and water with pulse lengths of 15 ms each, separated 8 s in time. From an atomic force microscope (AFM) image we can extract a root mean square (RMS) surface roughness of 0.5 nm of this layer, as shown in Fig. S2 (a). The actual layer thickness was found to be 197 nm.

On top of the oxide layer, a 150 nm thick film of gold is thermally evaporated in a physical vapor deposition (PVD) process. This layer serves as a broadband reflector. To ensure sufficient adhesion a 3 nm layer of chromium is deposited prior to the Au by e-beam evaporation. Deposition rates are tracked in-situ using a quartz crystal resonator and regulated using a PID controller to achieve 5 Å/s for Au and 2 Å/s for Cr. An AFM surface scan yields an RMS roughness of 1.8 nm.

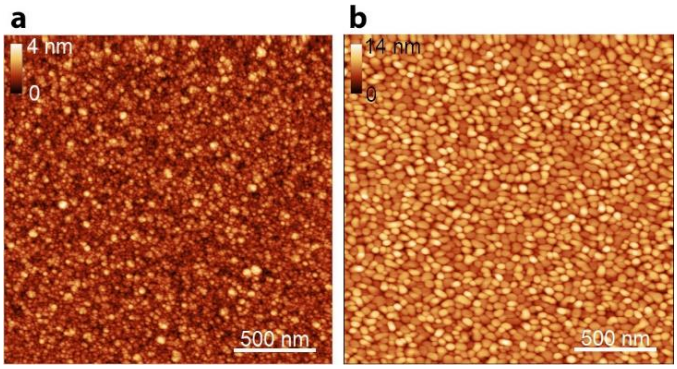

Figure S2 | (a) AFM scan of the Al_2O_3 layer deposited with ALD. **(b)** AFM scan of the Au layer deposited with PVD.

Flip-Chip stack bonding

Nanomembranes on a micro-machined piezo substrate can suffer from cracking when cooled to cryogenic temperatures when directly bonded to the substrate which makes an intermediate carrier sheet necessary for additional structural stability. We choose GaAs as "carrier sheet" to have the same thermal expansion coefficient of the QD membrane material and avoid mechanical stress to the membrane during the curing process (see below). In the first step, SU-8 is applied onto the gold surface of the sample with a brush and cured on a hot plate at 65 °C for 2 min and 95 °C for 5 min to evaporate solvents. Next, the temperature is raised to 130 °C to mobilize the solvents in the resist and contact is made with the polished surface from an equally sized piece of a bare GaAs wafer with a thickness of 350 µm utilizing a die bonding machine. Elevating the temperature to 230 °C for 10 min sparks crosslinking of the polymers in the resist, strongly bonding the two chips together.

Subsequently, the two-piece stack is lapped down from the GaAs new substrate side until this reaches a thickness of about 50 µm. For this step, the sample substrate acts as handle wafer. The stack is lapped parallel to the surface by a mixture of powdered Al_2O_3 and water as an abrasive.

By repeating the same bonding sequence, the carrier sheet is bonded onto the six-legged piezo such that it is stacked in between the upside-down sample and the piezo substrate.

Multi-step wet chemical etching

To remove the substrate used to grow the QDs, a four-step wet chemical back-etching process is employed, including a phosphorous acid solution for fast etching, timely changed to citric acid solution for selective etching stopping at the sacrificial layer and a subsequent removal of the sacrificial layer with hydrofluoric acid. Depending on environmental circumstances that cannot be controlled, residuals from the HF etching may possibly appear. These can be removed in potassium hydroxide.
For protecting the carrier sheet and the piezo substrate, the sample is glued to a Si chip carrier and protected on the sides using photoresist which is cured at 95 °C for 10 min on a hot plate.
The solutions are always freshly prepared. Volumetric mixing ratios include a 3:7 ratio of 85 % H_3PO_4 and 30 % H_2O_2 yielding a fast etch rate of approximately 5 µm/min when balancing the mixture for 15 min prior to etching and agitating the solution with a magnetic stirrer spinning at 150 rpm. The etching of the residual GaAs is obtained with a 1:4 ratio of H_2O_2 and powdered $C_6H_8O_7$ dissolved in a 1:1 mass ratio in water for slow but selective etching with a rate of 0.5 µm/min. The latter etchant is extremely selective against GaAs[1] and stops at the $Al_{0.75}Ga_{0.25}As$ layer. To remove the 400 nm thick sacrificial layer, etching in 10 % concentrated HF lasts only a few seconds. Residue from the sacrificial layer appearing on the sample surface are removed by dipping the sample in 44% KOH for 200 s.

Electron beam lithography and deposition of markers

To find the positions of QDs, a frame of reference is introduced, realized as metallic markers that are patterned using electron beam lithography (EBL). A film of 400 nm thick AR-P 6200.13 is spin-coated onto the sample surface and cured at 150 °C for 1 min on a hot plate. To avoid charging during the patterning, a 42 nm thick protective coating of AR-P 5090.02 is spun on the previous resist and cured at 90 °C for 1 min.

The design of the reference markers is patterned in EBL with an acceleration voltage of 30 kV, an aperture of 20 µm, and a dose of 65 µC/cm². The machine used is a Raith eLine system. After patterning, the protective resist is removed in a 1 min bath in de-ionized water and the e-beam resist is developed in AR 600-546 for 1 min. Development is stopped in isopropanol.

A stack of 50 nm Cr followed by 50 nm Au and again 50 nm Cr is deposited on the sample with the developed resist using PVD as described above. The use of a high atomic number element, such as Au, enables the detection of the markers using EBL with 100 kV acceleration voltage for deterministic patterning of photonic structures, while the symmetrized Cr layers serve for preventing the markers to curl, as well as for providing optical contrast with respect to the broadband reflector of the nanomembrane when illuminating with infrared (IR) light in the cryogenic microscopy setup used to measure single QD positions, see below. The reference markers are finished after a lift-off process in an alternate bath of anisole and acetone, as well as sonication.

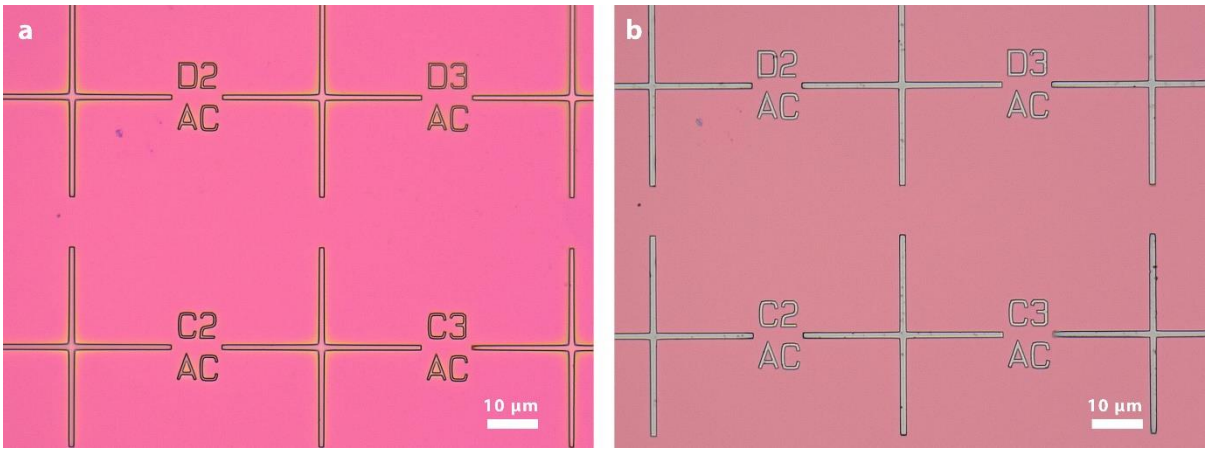

Figure S3 | Reference markers with a periodicity of 50 µm (a) after developing of the e-beam resist and **(b)** after metal evaporation and lift-off.

Imaging and QD position mapping

To acquire the QD positions through their photoluminescence (PL), the sample is placed in a continuous-flow cryostat and cooled with liquid He and imaged with a custom-built microscope, see sketch in Fig. S4a. To avoid contamination from the cryostat on the sample surface hindering subsequent processing steps, a protective layer of polymethylmethacrylate (PMMA) is applied. An 810 nm infrared (IR) light emitting diode (LED) illuminates the surface while a 470 nm blue LED simultaneously excites PL from the QDs. Metallic reference markers have Cr on the top, absorbing incident IR light and providing contrast to the reflective background (Au mirror placed below the AlGaAs membrane, which is transparent to the used IR light). QD PL emission is collected with a dichroic mirror with a cut-off wavelength of 650 nm. A glass-corrected near-IR optimized objective with a numerical aperture of 0.85 is used together with an achromatic lens doublet with a focal

length f = 100 mm to project an image with a magnification of 57 onto a monochromatic CMOS active pixel type solid-state image sensor with a pixel size of 2.9 x 2.9 µm² and a resolution of 1936 x 1096 pixels, operated with low gain and an exposure time of 1 s. Spectroscopy on single QDs is performed by using a 532 nm green diode laser and diverting the signal toward a spectrometer. Using the PL emission of QDs for characterizing the point spread function (PSF) of the imaging system under the same conditions as used to record images, we find that light from the QDs appears as Airy discs with a full width at half maximum (FWHM) of 520(25) nm (statistical value of 372 QDs), which corresponds to a value 1.11(5) larger than the anticipated value of the diffraction limit of the objective lens:

$$\mathrm{FWHM}_{\mathrm{lateral}} = 0.51\,\frac{\lambda}{\mathrm{NA}}\,.$$

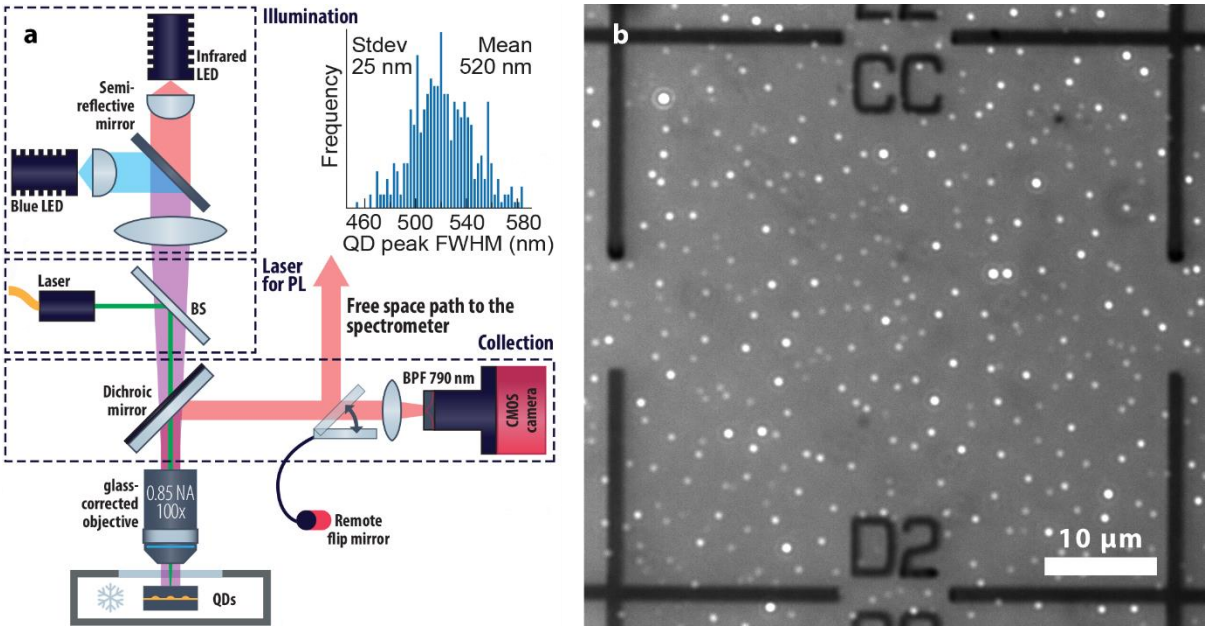

Figure S4 | (a) A sketch of the PL imaging setup with IR and blue LEDs for surface illumination and PL excitation, a fibre-coupled laser for µ-PL of single QDs and collection using a dichroic mirror and a band-pass filter for imaging on a monochromatic CMOS camera. The inset shows a histogram of the FWHM of the central peak of Airy discs corresponding to the PL of different QDs. The mean value of the FWHM is 520(25) nm. **(b)** Example of image of excited QDs and illuminated sample surface.

QD positions with respect to the frame of reference of the metallic markers are extracted from the image by using a script for numerical image processing including a Hough transformation for finding the markers, a Gaussian fit perpendicular to the lines of the marker to refine their detection, as well as a peak finder with 2D Gaussian fits for finding the peak position of each single QD emission spot.

A statistical method is employed to estimate the random and numerical error of QD positions with respect to the reference markers. To generate data, 30 images of the same marker field are taken, and the position mapping script is applied to each of them, yielding the arithmetic mean position as well as the standard deviation for x and y coordinates for each QD position. The standard deviation of the Euclidian distance to the mean can be calculated through the addition of the variances in both directions, as

$$\sigma_r = \sqrt{\sigma_x^2 + \sigma_y^2}\,,$$

which provides one σ_r for each QD position. Those deviations are counted in a histogram binned into 1 nm columns. A fit of such data containing 284 data points using a log-normal distribution shows a peak at 18 nm, whereas the median of the data set is 22 nm. With numerical image pre-processing such as thresholding, brightness control and rescaling intensity values, the peak of the log-normal fit on 280 data points can be reduced to occur at 10 nm, while the median is 15 nm.

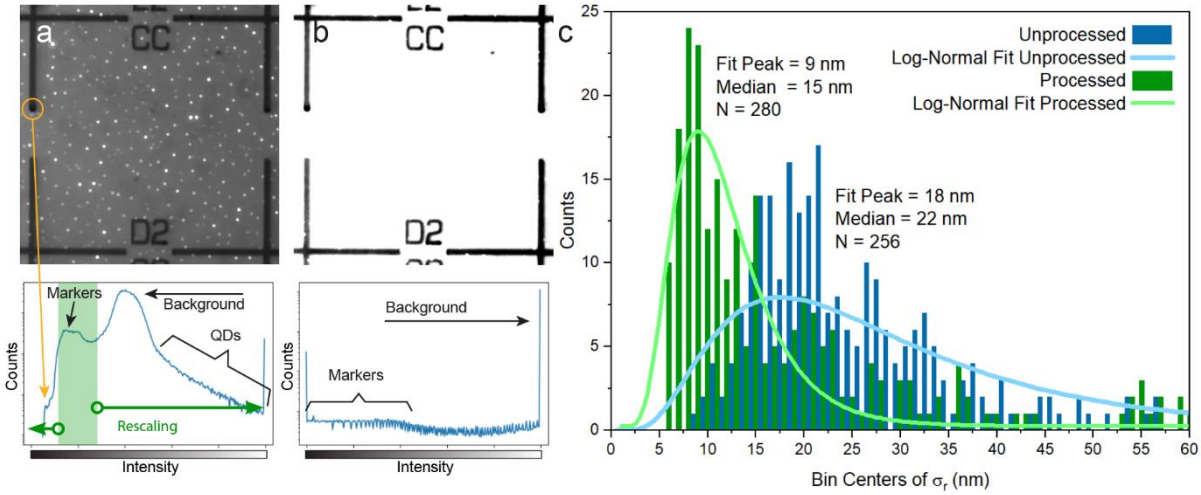

Figure S5 | (a) Recorded image of markers and QDs with its corresponding intensity histogram in logarithmic scale (bottom). Dark/bright pixels in the image correspond to bins in the left/right part of the histogram, as indicated by the intensity scale. Pixels corresponding to the markers yield the peak marked in green in the histogram with a side peak to the left stemming from dark spots in the image of markers. **(b)** Through rescaling the green area of (a) to full range, QDs which are parasitic in the marker detection process can be removed, and the contrast of markers and background can be maximized, as well as the markers' internal structure reduced. **(c)** Histogram of the standard deviations of the Euclidian distance σ_r to the mean of *N* QD positions. "Unprocessed" corresponds to marker detection performed in the image from panel (a), whereas "Processed" belongs to marker detection performed in the image of panel (b).

Calibration of cavity mode position

Due to layer-thickness gradients occurring during the epitaxial growth and oxide deposition, the cavity mode of a given CBR design shifts in its spectral position depending on the lateral position of the CBR on a sample. Therefore, a calibration of the central disc radius of the CBR turned out to be necessary. Light from a white light source is focused to a spot impinging in the centre of a CBR structure at room temperature. The reflected signal is normalized by the reflection of the spot outside of such a structure on the nanomembrane. Reflectivity spectra are shown in Fig. S6 and the dependency on the centre disc radius is extracted. To match the mode position with the emission of QDs at cryogenic temperatures, a blue-shift of the cavity mode of 10 nm needs to be considered, as extracted by temperature-dependent measurement of the cavity mode, not shown here.

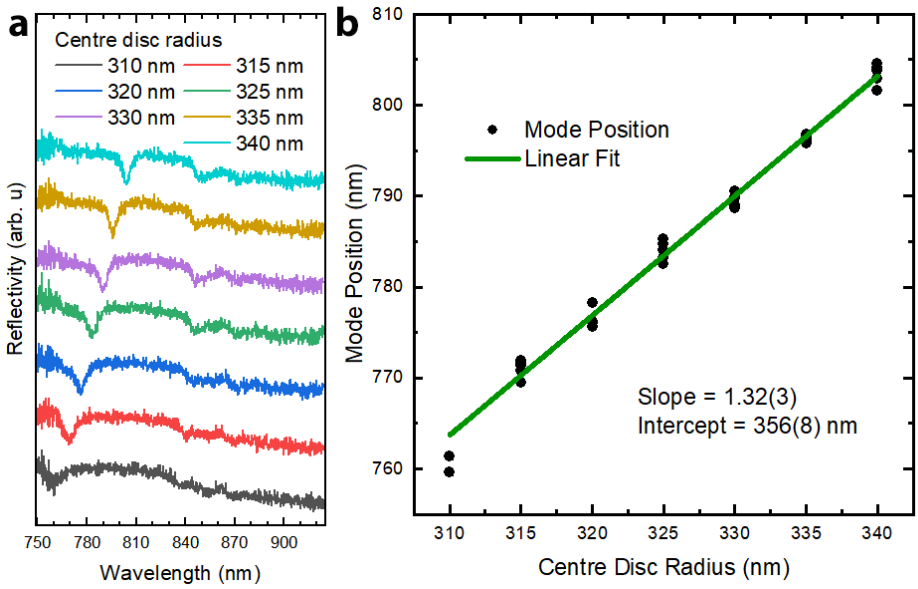

Figure S6 | (a) µ-reflectivity spectra of several structures fabricated for calibration on the same chip. The mode is visible as a reflectivity dip moving towards higher wavelengths for larger centre disc radii. **(b)** A linear fit is used to recreate the desired wavelength.

Deterministic fabrication of CBR structures

CBR cavities are fabricated deterministically on QD sites with tailored mode positions for certain single QDs. If no spectral information of a QD is available, CBR cavities are equally distributed with target mode positions at X + 1 nm, X + 3 nm, and X - 1 nm, where X is the mean spectral position of the excitonic transition on the sample. Position and geometry of CBR structures are provided to a Jeol JBX-9300FS 100 kV EBL system which aligns to the frame of reference induced on the sample through the deposited metallic markers. The intermediate Au layer interacts with the electron beam providing contrast to the semiconductor surface. The EBL system aligns the internal coordinate system using perpendicular line scans on the lines of the marker crosses. The design is then transferred onto an approximately 550 nm thick layer of PMMA resist serving as a mask for reactive ion etching (RIE) using an inductively coupled plasma (ICP) source. CBR structures are etched using a Cl_2 and Ar mixture (1.7 sccm to 18 sccm) with a 10 mTorr pressure, a radio-frequency (RF) power of the substrate electrode of 50 W, an ICP power of 150 W, and a bias voltage of 250 V yielding a roughly estimated etch rate of 85-100 nm/min.

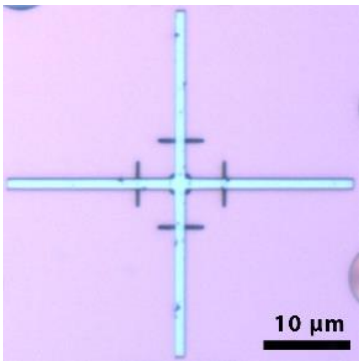

Figure S7 | Four-line scans of the e-beam perpendicular to the marker cross lines and a square scan in the centre of the cross. Exposed areas of the resist due to the scan are developed and the underlying AlGaAs layer dry-etched as well.

To estimate the precision of EBL-assisted deterministic patterning we compare the position of detected QDs with the position of deterministically patterned Au discs. On an as-grown sample, i.e., no nanomembrane, approximately 100 QD positions are recorded per each of 221 marker fields to pattern gold discs with radii distributed among 150 nm and 500 nm on QD sites using the Raith eLine 30 kV EBL system. A subsequent metallization, lift-off, and imaging of all Au discs through reflectivity yields the positions of those discs with respect to the reference markers using the same script as used for QDs. An image of a marker field with 100 detected QDs, an image of the same marker field but with Au discs, as well as a histogram of the count of Euclidian distances Δ*r* between centres of corresponding Au discs and QDs is provided in Fig. S8, yielding an estimated patterning accuracy of 33 nm (position of the peak of the Log-Normal fit), while the median of Δ*r* values is 43 nm.

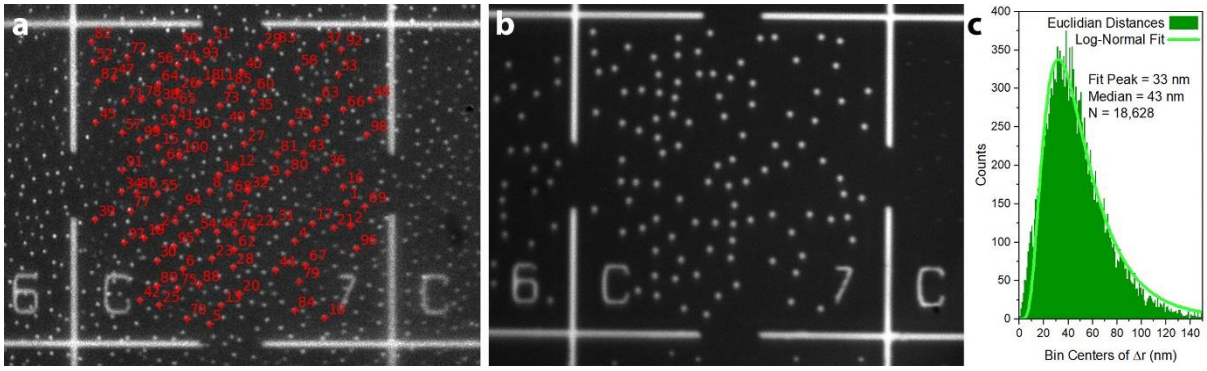

Figure S8 | (a) Au markers reflecting the IR LED and PL of QDs excited by a blue LED. A set of 100 QDs was recorded for each marker field. **(b)** Au markers and Au discs on pre-recorded QD sites, both reflecting the IR LED. **(c)** Histogram of the Euclidian distances Δ*r* between the centers of QDs and Au discs using 18,628 data points.

S2 | Cavity mode characterization at low temperature

The mode of a cavity is characterized in a cryostat at low temperature (5K) by focusing a white halogen lamp (3000K) on the sample through a 0.5 NA aspheric lens and collecting light from the centre of the cavity with a single mode fibre. The collected spectra are normalized with the flatfield response of the system obtained by shining the same light on a highly reflective part of the sample (namely the unprocessed membrane). The two reflectivity spectra for the cavities containing QD2 and QD4 discussed in the main text are shown in Fig. S8, panels a and b, respectively. The emission from the QD states excited by the white lamp is also visible in the reflectivity spectra. The detuning from the cavity mode centre influences the magnitude of the Purcell factor. As expected, a lower detuning, as for QD2 in panel a of Fig. S9, produces a higher Purcell factor.

From a Fano fit of the cavity mode it is possible to extract the quality factor (Q) of the cavity. The extracted values, 115(1) and 104(1) for the CBRs with QD2 and QD4, respectively, are slightly lower than the expected values for this type of structure (150) but comparable in order of magnitude.

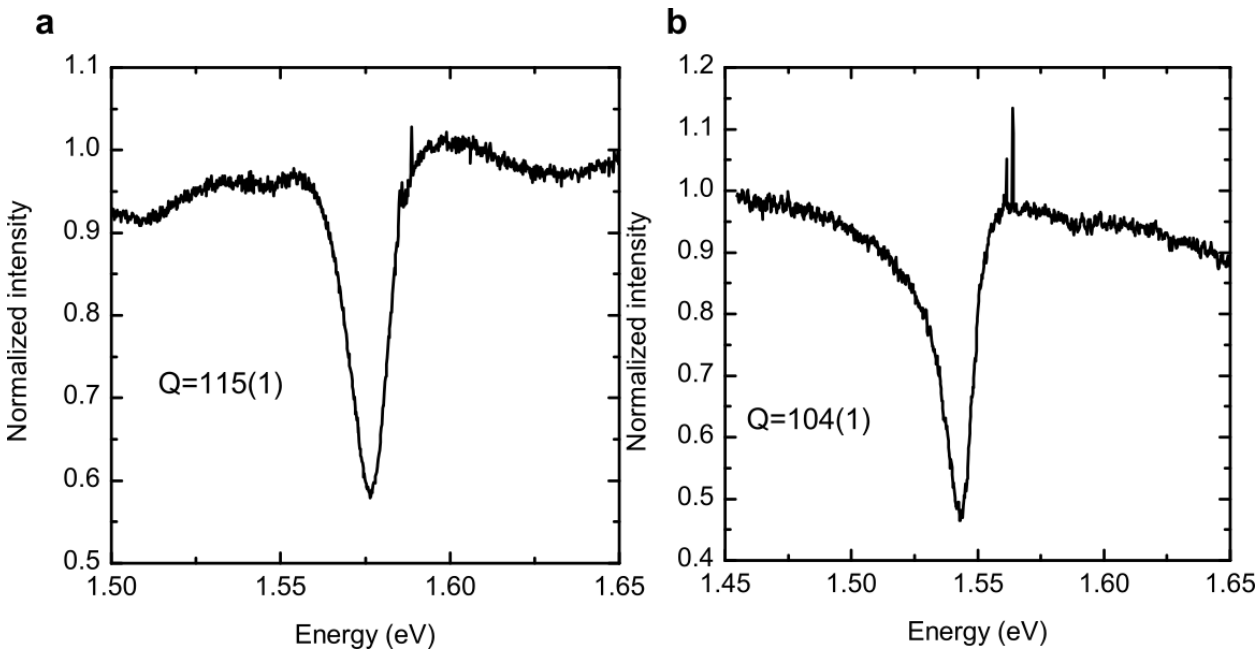

Figure S9 | Normalized low temperature reflectivity spectra of the CBRs containing QD2 (a) and QD4 (b). The quality factor is calculated from a Fano resonance fit of the cavity mode dip[2].

S3 | Lifetimes

The lifetime measurement setup and conditions are described in detail in the Methods section of the main text. In Fig. S10 we report the time-resolved PL traces for QD2 and QD4, panel (a) and (b) respectively. The values of the lifetime for X and XX are extracted by fitting the experimental curves with an exponential decay and instrument response function (IRF) convolution and are reported in figure.

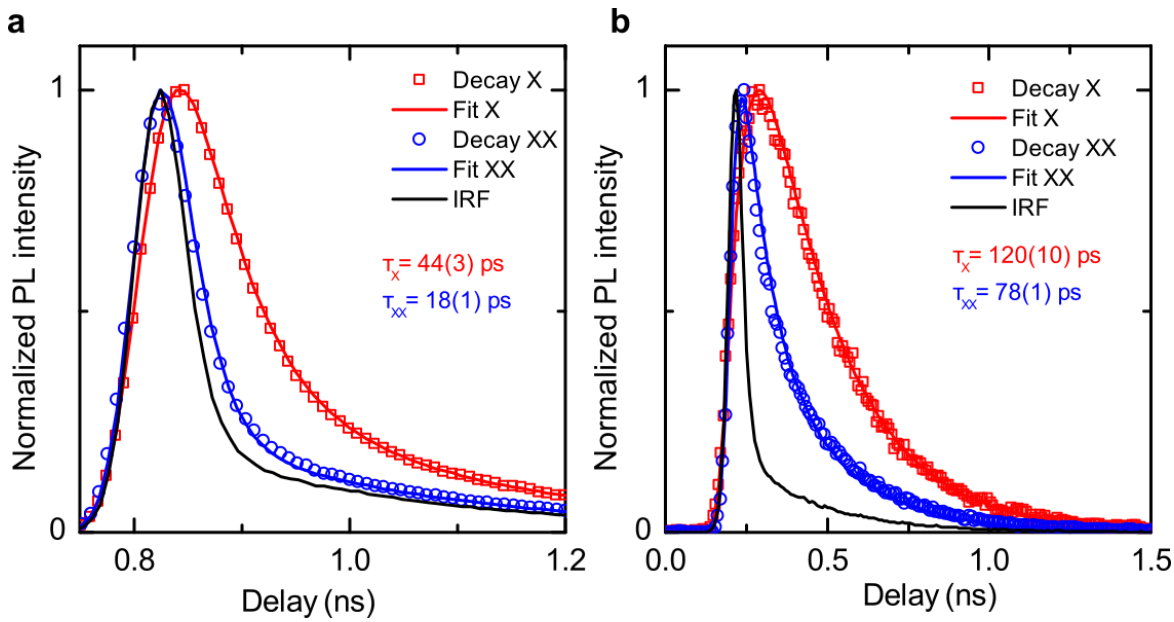

Figure S10 | Time-resolved photoluminescence of the X (red squares) and XX (blue circles) transition intensities from QD2 **(a)** and QD4 **(b)**, and instrument response function (IRF) (black solid line) of the setup. The lifetime values are obtained with a fit (solid lines) convoluting the IRF with the exponential decay functions expected from the radiative cascade.

S4 | Rabi oscillations

The signal of the X line of the brightest QD in the sample, excited with TPE, is coupled into a multimode fibre and sent to a silicon avalanche photodiode (APD). The number of counts per second on the APD is recorded while increasing the power of the laser used for TPE. The Rabi oscillations in the intensity are a clear signature of the resonant excitation.

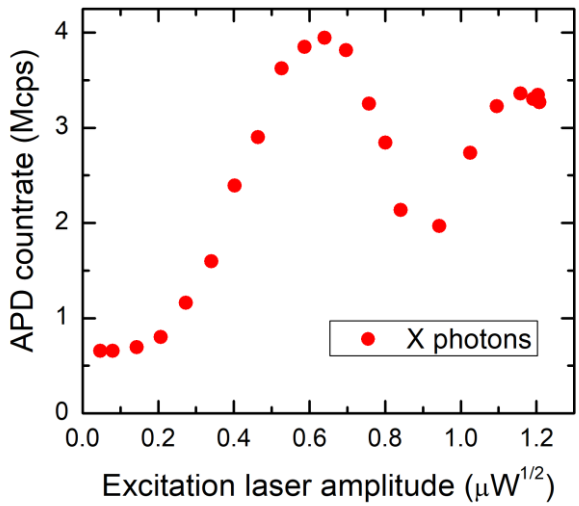

Figure S11 | Count rates on the avalanche photodiode for the X transition coupled in a multimode fibre as a function of the excitation power of the two-photon resonant laser. The non-zero intensity at null laser power is attributed to above-band excitation due to the white light used to neutralize the QD.

S5 | Extraction efficiency

To calculate the extraction efficiency, we measure the photon rates at the APDs at π-pulse and quantify all the other figures that contribute to the observed photon rates: the efficiency of the excitation, the transmission through the optical elements of the setup, the fibre coupling efficiency, and the efficiency of the detectors.

The measured photon rates of the X and XX are corrected to isolate only the contribution from the two-photon cascade: we subtract from the counts of the X channel the number of photons which are emitted by above band excitation from the white halogen lamp shining on the sample to neutralize the QD and enable the TPE (see the non-zero counts at null laser power in Fig. S11), while we subtract from the XX channel counts the contribution from an emission line close to the XX, whose ratio is calculated from the spectrum of the signal going to the APD.

The pair emission probability η_{pair} is the combination of the preparation fidelity of the TPE η_{prep}, i.e., the probability that the laser pulse excites the QD when it is sitting in its charge-neutral ground state, and the blinking ratio η_{blink}, i.e., the fraction of time that the QD is optically active (in its charge-neutral ground state). η_{pair} is calculated from the corrected, see previous paragraph, single photon count rates of the X and XX channels ($\tilde{R}_X$ and $\tilde{R}_{XX}$) and the coincidences between the two channels (n_c) multiplied by the laser repetition rate (the rates were all measured in single mode fibres):

$$\eta_{pair} = \frac{\tilde{R}_X \cdot \tilde{R}_{XX}}{n_c \cdot \mathrm{R}_{laser}} = \frac{1.75(1)\ Mcps \cdot 1.98(1)\ Mcps}{0.155(1)\ Mcps \cdot 80\ Mcps} = 0.279(3)$$

and contains also any non-radiative channel and the quantum efficiency of the process. By estimating the average blinking fraction $\eta_{blink} = 0.29$ from long time range $g^{(2)}$ measurement we can calculate the preparation fidelity as $\eta_{prep} = 0.96$.

The losses on the bulk optics were estimated via direct measurement of the power of a laser beam with the same wavelength of the QD emission passing along the same path as the signal from the QD. The components comprise an aspheric lens, two windows of the cryostat, a two-lenses telescope to reduce the beam size, a 90:10 beam splitter, two notch filters, a long pass 750 nm filter, the two volume Bragg gratings (VBG) notch filters used to reflect only the X and XX lines, four metallic high-reflection mirrors and one dielectric mirror. The setup transmission was measured as $\eta_{setup}^{X} = 0.60(2)$ and $\eta_{setup}^{XX} = 0.62(2)$.

The multimode fibre coupling efficiency, $\eta_{FC,MM} = 0.929(3)$, was estimated by measuring the laser power before the fibre coupler and at the exit of the fibre. The single mode fibre coupling efficiency was derived by comparing the count rates of the detectors in multimode fibre and in single mode fibre measured under the same conditions.

To calculate the actual efficiency of the detectors $\tilde{\eta}_{det}$ we must correct the efficiency given by the manufacturer, $\eta_{det} = 0.46$, for the non-linearity due to the detector dead time $\tau_{det} = 34\ ns$. The correction factor is obtained by observing the change in intensity of the signal while placing neutral density filters with different optical density in front of the detectors, calibrated at the correct wavelength. The corrected efficiency values obtained are $\tilde{\eta}_{det}^{X} = 0.379(2)$ and $\tilde{\eta}_{det}^{XX} = 0.410(2)$. If we estimate the expected detector efficiency based on the observed count rate and on the dead time, including a first order non-linearity correction:

$$\tilde{\eta}_{det} = \eta_{det} \cdot \left(1 - \tau_{det} \cdot R_{QD}\right)$$

we observe a difference with respect to our experimental estimate. This discrepancy is arguably to be ascribed to the blinking of the QD. We model the blinking using a telegraphic model in which the QD either emits light (on) or does not emit light (off), staying on for an average time τ_{blink} and for a fraction of total time η_{blink}. Due to this effect, if τ_{blink} is higher or comparable to τ_{det}, the detectors receive a photon flux which is much higher than the average value measured, when the QD is on, and no photons when the QD is off. The non-linear response of the detector must then be corrected for the actual value impinging on the sensor during the on-time of the QD, also considering the interplay between the deadtime of the detector τ_{det} and the switching time of the QD τ_{blink}. The detector efficiency can then be corrected in the case of a blinking QD by adding a multiplicative factor on the actual count rate:

$$\tilde{\eta}_{det} = \eta_{det} \cdot \left(1 - \tau_{det} \cdot \frac{R_{QD}}{c_{blink}}\right)$$

Here, c_{blink} has an average value of ~ 0.7, which is higher than the estimated η_{blink}. This is because $\tau_{blink} = \sim 60\ ns$ is close to τ_{det} so that only the slower blinking components contribute to the increase in the effective photon flux seen by the detectors. This figure can be associated with the drop in coincidences at the delays longer than the detector dead time in the intensity autocorrelation function. By correcting the measured rate at the APDs with $\tilde{\eta}_{det}$ we can also obtain

the actual average photon flux impinging on the APDs in multimode fibre as $R_{QD,MM} = \frac{R_{APD,MM}}{\tilde{\eta}_{det}} = 9.6(1)$ Mcps.

The extraction efficiency can be then finally calculated from the formula:

$$R_{APD} = R_{laser} \cdot \eta_{pair} \cdot \eta_{ext} \cdot \eta_{setup} \cdot \eta_{FC} \cdot \tilde{\eta}_{det}$$

as:

$$\eta_{ext} = \frac{R_{APD}}{R_{laser} \cdot \eta_{pair} \cdot \eta_{setup} \cdot \eta_{FC} \cdot \tilde{\eta}_{det}}$$

Table S1 | Measured photon rates and efficiencies of the different parts of the experimental setup for the X and XX emission channels.

	$\tilde{R}_{APD,SM}$ (Mcps)	$\tilde{R}_{APD,MM}$ (Mcps)	R_{laser} (Mcps)	η_{pair}	η_{setup}	$\eta_{FC,SM}$	$\eta_{FC,MM}$	$\tilde{\eta}_{det,SM}$	η_{ext}
X	1.75(1)	3.13(1)	80	0.279(3)	0.60(2)	0.511(4)	0.929(3)	0.379(2)	0.67(3)
XX	1.98(1)	3.52(1)			0.62(2)	0.508(5)		0.410(2)	0.69(4)

S6 | FSS erasure

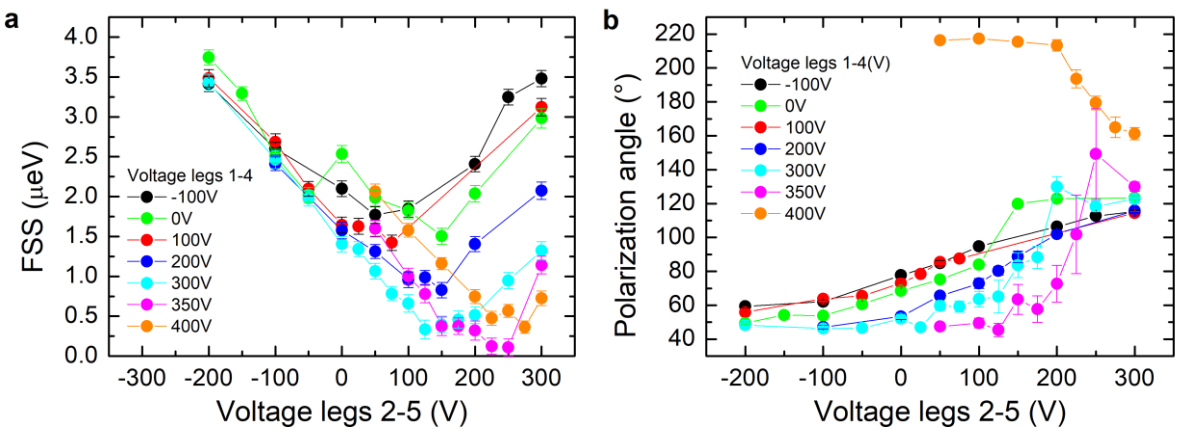

Figure S12 | (a) Fine structure splitting (FSS) and **(b)** polarization angle vs applied voltage on the piezoelectric actuator legs of QD2.

The FSS erasure procedure was replicated on QD2 by exchanging the sweep order of legs 1-4 and 2-5. Fig. S12 shows the amplitude of the FSS and the polarization angle for several sweeps on legs 2-5 while changing the voltage of legs 1-4. The voltage sweep corresponding to the minimum of the FSS is the pink one. The minimum value is obtained for a voltage on legs 1-4 of 350V and 250 V on legs 2-5, which are compatible with the conditions found previously for a minimum on the same QD, as shown in Fig. 3a of the main text. Increasing the voltage of legs 1-4 beyond this point produces a flip in the angle of the polarization (orange curve), confirming that the minimum condition is surpassed[3].

References

1. Tong, M. *et al.* A comparative study of wet and dry selective etching processes for GaAs/AlGaAs/InGaAs pseudomorphic MODFETs. *J. Electron. Mater.* **21**, 9–15 (1992).

2. Krieger, T. M. *et al.* Postfabrication Tuning of Circular Bragg Resonators for Enhanced Emitter-Cavity Coupling. *ACS Photonics* **11**, 596–603 (2024).

3. Trotta, R. *et al.* Universal Recovery of the Energy-Level Degeneracy of Bright Excitons in InGaAs Quantum Dots without a Structure Symmetry. *Phys. Rev. Lett.* **109**, 147401 (2012).